

Pressure Dependent Yields and Product Branching Ratios in the Broadband Photolysis of Chlorine Nitrate

Scott L. Nikolaisen,¹ Stanley P. Sander² and Randall R. Friedl
Jet Propulsion laboratory, California institute of Technology
4800 Oak Grove Drive, Pasadena, CA 91109

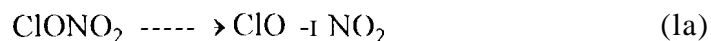
11/29/95

1) Permanent address: Department of Chemistry and Biochemistry, (California State University,
Los Angeles, 5151 State University Drive, Los Angeles, CA 90032

2) Author to whom correspondence should be addressed

Abstract

The photolysis of chlorine nitrate was studied using broadband flash photolysis coupled with long-path ultraviolet-visible absorption spectroscopy. Branching ratios for the $\text{Cl} + \text{NO}_3$ and $\text{ClO} + \text{NO}_2$ product channels were determined from time-dependent measurements of ClO and NO_3 concentrations. Yields of the ClO and NO_3 products displayed a dependence on the bath gas density and the spectral distribution of the photolysis pulse. Product yields decreased with increasing bath gas density regardless of the spectral distribution of the photolysis pulse, however the decrease in product yield was much more pronounced when photolysis was limited to longer wavelengths. For photolysis in a quartz cell ($\lambda > 200 \text{ nm}$) the yield decreased by a factor of two over the pressure 10-100 Torr. in a Pyrex cell ($\lambda > 300 \text{ nm}$), the yield decreased by a factor of 50 over the same pressure range. When photolysis was limited to $\lambda > 350 \text{ nm}$, the yield decreased by a factor of 250. Branching ratios for the photolysis channels



were determined from the relative ClO and NO_3 product yields at various pressures. Although the absolute product yield displayed a pressure dependence, the branching between the two channels was independent of pressure. The branching ratios are $\beta_{1a} = 0.6102 \pm 0.059$ and $\beta_{1b} = 0.390 \pm 0.059$ for photolysis with $\lambda > 200 \text{ nm}$, and $\beta_{1a} = 0.440 \pm 0.070$ and $\beta_{1b} = 0.5603 \pm 0.070$ for photolysis with $\lambda > 300 \text{ nm}$. The implications of these results for the chemistry of the lower stratosphere are discussed.

I. Introduction

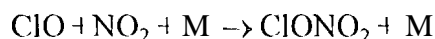
The photolysis of chlorine nitrate (ClONO_2) may proceed through one of several bond cleaving processes, the most likely being



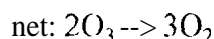
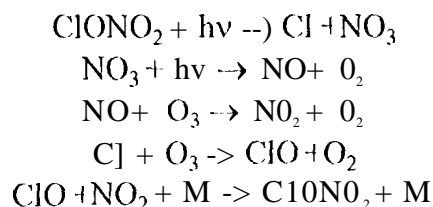
where λ_{thresh} is the threshold wavelength for the indicated channel. The quantum yields of the radical product channels, the wavelength dependence of the dissociation rate, and the possible effects of bath gas collisions are measurements which provide information about the detailed dynamics of the dissociation process. A number of previous studies have examined the branching ratios among the various dissociation pathways.¹⁻⁹ In 1983, Margitan reported that branching among the possible product channels was dominated by reaction 1b with 90% of dissociation occurring via this process and the remaining 10% proceeding via reaction 1c at 266 nm and 355 nm.⁶ He saw no evidence of the ClO product from reaction 1a even though dissociation via this channel cleaves the weakest bond in the molecule. These values have served as the basis for recommendations for atmospheric modeling calculations. In a recent set of experiments, Minton *et al.* photolyzed ClONO_2 in a molecular beam and detected the products with time- and angle-resolved mass spectrometry.⁸ They reported nearly equal branching ratios for channels 1a and 1b when photolyzing at 248 nm, and the branching favored channel 1b by a ratio of ~2:1 when photolyzing at 193 nm. They found no evidence of reaction 1c at either photolysis wavelength and placed an upper limit on this channel of $< 4\%$.

Graña *et al.* have recently performed *ab initio* calculations on ClONO_2 using configuration interaction methods with a large basis set.¹⁰ Vertical excitation energies were calculated for several electronic states in the singlet and triplet manifolds, and oscillator strengths were determined for singlet-singlet transitions. This work has helped to identify the electronic states involved in ClONO_2 photodissociation and have permitted the assignment of several of the bands observed in the ultraviolet absorption spectrum.

Recent interest in chlorine nitrate stems from its involvement in the chemistry of the stratosphere. ClONO₂ is produced by the recombination reaction



and is an important temporary reservoir of inorganic chlorine in the lower and middle stratosphere. The most significant loss mechanism for ClONO₂ is photodissociation, and the relative photolysis quantum yields have implications for the production and loss of ozone. While photolysis pathway 1a results in a null cycle, photodissociation via pathway b results in a catalytic cycle for ozone loss:



This cycle is particularly important at the edges of the polar winter vortex.

While the relative quantum yields are important for atmospheric modeling, the absolute magnitude of the ClONO₂ photodissociation rate is also important insofar as it determines the partitioning of inorganic chlorine between ClONO₂ and HCl in the lower and middle stratosphere. The first-order photolysis rate constant, J_{ClONO_2} , is given by

$$J_{\text{ClONO}_2}(z) = \int I_{\text{solar}}(\lambda, z) \sigma_{\text{ClONO}_2}(\lambda) \Phi(\lambda) d\lambda$$

where $I_{\text{solar}}(\lambda, z)$ is the solar flux at wavelength λ and altitude z , $\sigma_{\text{ClONO}_2}(\lambda)$ is the absorption cross section, and $\Phi(\lambda)$ is the quantum yield for photodissociation into all radical channels. Below 28 km, solar radiation is restricted primarily to wavelengths longer than about 290 nm. As a result of the rapidly decreasing ClONO₂ cross section and increasing solar flux at wavelengths longer than this cutoff, the product $I\sigma\Phi$ maximizes at about 330 nm. However, laboratory measurements of ClONO₂ quantum yields usually take place at much shorter wavelengths to take advantage of the larger absorption cross sections. Atmospheric model calculations have adopted these quantum yields under the assumption that they also apply in the spectral region beyond 290 nm. This assumption may be incorrect if, for example, excitation in the long wavelength tail of

ClONO_2 results in intersystem crossing to the triplet manifold. The formation of metastable triplet states could decrease the effective value of J_{ClONO_2} if collisions] de-excitation can compete with dissociation. In the atmosphere, this would have the effect of reducing $[\text{Cl}]$ and increasing ClONO_2 at the lower altitudes.

We have performed an extensive set of measurements on the dissociation of chlorine nitrate in order to determine the product branching ratios and yields as functions of photolysis wavelength and pressure. The technique employed a broadband flashlamp for photolysis and long path [UV/visible absorption to detect the products. Section II describes the experimental apparatus and data acquisition. Section III outlines the results including the branching ratios into the different product channels as a function of wavelength and the dependence of the product yield on the total pressure within the reaction cell. Section IV presents a mechanism for dissociation which qualitatively simulates the essential features of the data. A brief discussion of the implication for stratospheric chemistry is also presented.

II. Experimental

The flash photolysis/long path UV-visible absorption apparatus and basic techniques employed in these experiments have been described in detail previously,¹² and only those points unique to this study will be emphasized. Chlorine nitrate was synthesized by the reaction of Cl_2O with N_2O_5 . Cl_2O was made using the method of Cady¹² in which a 10-20% mixture of Cl_2 in helium was slowly flowed over dried HgO supported on 4 mm glass beads. The reaction was carried out at a total pressure of 250 Torr. Product Cl_2O and unreacted Cl_2 were collected at 161 K in an ethanol/ $\text{N}_2(\text{l})$ trap. Cl_2O was purified by vacuum distillation at 195 K (*iso*-propanol/ $\text{CO}_2(\text{s})$ slush) until Cl_2 was undetectable as observed by monitoring the UV absorption band centered at 325 nm. N_2O_5 was produced from the reaction of NO_2 and O_3 . A slow flow of neat NO_2 was combined with O_3 from an ozonizer and allowed to react in a 9 mm tube 21 cm in length. N_2O_5 was collected in an *iso*-propanol/ $\text{CO}_2(\text{s})$ trap. The flow of NO_2 was adjusted so that the reaction ran to completion within the length of the tube.

Chlorine nitrate was produced by transferring under vacuum a small amount of Cl_2O into the container of N_2O_5 . The container was slowly warmed to 273 K at which temperature the reaction of Cl_2O with N_2O_5 to form ClONO_2 is complete. This process of adding Cl_2O to the $\text{N}_2\text{O}_5/\text{ClONO}_2$ container was repeated until only a small amount of N_2O_5 remained. By leaving an excess of N_2O_5 relative to Cl_2O , it was assured that there would be no Cl_2O impurity in the ClONO_2 sample. ClONO_2 was separated from N_2O_5 by vacuum distillation to a 195 K bubbler. Finally, the chlorine nitrate sample was checked for Cl_2 impurity by monitoring the chlorine absorption band centered at 325 nm. No perceptible impurities were detected.

Two reaction cells with identical geometry were used in this study. One was constructed of quartz and the other from Pyrex glass. The reaction cells consisted of a 30 mm id, x 90.5 cm cylindrical tube surrounded by three annular jackets. The outermost jacket was connected to a chiller/heater circulator to allow temperature control of the reaction. The temperature within the reaction cell was varied from -253 K to 400 K. The middle jacket comprised the flash lamp. This jacket was connected to a high voltage power supply via tungsten electrodes and was filled with 30 Torr xenon. 27.5 kV was discharged from a 2.4 μF capacitor through the xenon gas to produce a broadband flash of light 10-20 μs in duration. The innermost jacket was used to spectrally filter the output of the xenon flash lamp by the use of inorganic salt solutions. The use of different cell materials also allowed spectral selection of the short wavelength cut-off of the photolysis source. The Pyrex cell did not transmit light at wavelengths shorter than 300 nm, but the quartz cell transmitted light down to approximately 200 nm.

Flash lamp spectral distributions were obtained by imaging the scatter-cd light exiting the reaction cell windows onto a 0.3 m monochromator that was equipped with a 1024 pixel diode array detector. A 1200 line mm^{-1} grating blazed at 250 nm was used for the spectral measurements which resulted in a spectral bandpass of approximately 60 nm. To obtain the complete spectral distributions from 200 nm to 450 nm (the region over which chlorine nitrate has measurable absorption cross sections accessible in these experiments) it was necessary to scan the monochromator in 50 nm steps, collect the scattered light data, and splice the measured spectra together. Absolute wavelength calibration was provided by a mercury pen ray lamp. Spectral distributions for the unfiltered photolysis light in the quartz and Pyrex cells are shown in

Figure 1. Solutions of chromium potassium sulfate ($\text{CrK}(\text{SO}_4)_2 \cdot 12\text{H}_2\text{O}$, $100 \text{ g l}^{-1} \text{ H}_2\text{O}$) and ceric ammonium nitrate ($\text{Ce}(\text{NH}_4)_2(\text{NO}_3)_6$, $5 \text{ g l}^{-1} \text{ H}_2\text{O}$) were also used in the Pyrex cell filter jacket to provide further spectral selection of the photolysis light. Spectral distributions for these salt solutions are also shown in Figure 1. The overlap of the spectral distributions from the four cell/filter combinations with the ClONO_2 absorption spectrum is shown in Figure 2.

Chlorine nitrate was introduced into the reaction cell by passing helium (99.999%) through a bubbler containing pure ClONO_2 liquid at 195 K (*iso*-propanol/ $\text{CO}_2(\text{s})$ slush). The backing pressure of helium was set at 510 or 1020 Torr depending on the desired ClONO_2 concentration in the reaction cell. Bath gas was added to the ClONO_2 /helium mixture prior to entrance into the reaction cell to allow complete mixing of all gases. Species concentrations were determined using calibrated mass flow meters, and flow rates of each gas were adjusted in order to maintain the desired total pressure and ClONO_2 concentration. The pressure of the reaction cell was measured with a capacitance manometer and maintained at a preset value by means of an automated control valve at the cell exit to the vacuum pump.

The mechanism of chlorine nitrate photolysis were studied by monitoring the ClO and NO_3 products. ClO and NO_3 were monitored by UV/visible absorption spectroscopy in which the collimated output of a 150 W xenon arc lamp was passed through the reaction cell using White-type optics to achieve a total optical path length of 724 cm. For those measurements in which high temporal resolution was desired, the arc lamp beam was directed to a 0.5 m monochromator equipped with a photomultiplier tube (PMT). The slits of the single wavelength PMT spectrometer were 150 μm . For ClO detection, the spectrometer was equipped with a 2400 line mm^{-1} grating blazed at 300 nm. The spectrometer was tuned to the $\text{A}^2\P(1(v' = 12) \leftarrow \text{X}^2\P(1(v'' = 0))$ vibrational band at 275.3 nm. The light intensity was measured with a 166U11 PMT. The PMT signal was passed to an amplifier which had a variable low-pass filter. The amplified signal was digitized and signal-averaged using a 100 kHz digital oscilloscope. For the NO_3 product, a 1200 line mm^{-1} grating blazed at 500 nm and a R955 PMT were used. The spectrometer was tuned to the $\text{A} \leftarrow \text{X}$ transition at 662 nm.

ClO and NO_3 were also monitored using a 0.3 m monochromator equipped with a 1024 pixel diode array detector. This detector required a minimum of 16.67 ms to read and store data

from all pixels of the array. The minimum time required to scan the array could be shortened by reading only a subset of the array pixels: for example, the time resolution was reduced to 5 ms by reading only 270 consecutive pixels. For ClO detection, a 2400 line mm⁻¹ grating was used which resulted in a spectral bandpass of 30 nm. The grating was tuned to 280 nm which lies in the middle of the A²Π←X²Π vibrational progression. For NO₃, a 1200 line mm⁻¹ grating with a spectral bandpass of 60 nm was tuned to 640 nm where the prominent A←X (0,0) and (1,0) vibration transitions could be simultaneously detected. This spectrometer offered increased sensitivity for both ClO and NO₃ over the single wavelength spectrometer because of the multiplex advantage of using the diode array detector, but sensitivity was gained at the expense of temporal resolution. The sensitivity was increased over the PMT spectrometer because each scan of the array produced a portion of the absorption spectrum of ClO or NO₃. The experimental spectrum was then fit to a reference spectrum using a least-squares routine. Reference spectra were created by averaging 1000 scans of the diode array collected under conditions in the reaction cell which maximized the production of either ClO or NO₃. The reference spectrum was then compared to the known cross section to calculate the concentration of the product species in the reference spectrum. The cross sections for ClO were those of Sander and Friedl,¹¹ and the NO₃ cross sections were taken from Sander.¹³ The fitting routine directly determined the concentration of the species being detected from the absorption spectrum recorded by the diode array,

Temporal information on the formation and decay of the product signals measured with the diode array spectrometer was obtained by successive scans of the array. The array interface electronics allowed for the acquisition, co-addition, and storage in dedicated memory locations of up to 512 separate scans of the array each time the flash lamp fired with each scan accounting for a 5-16.67 ms portion of the signal waveform dependent on the number of pixels read. Each of the 512 scans, which consisted of the spectrum of the particular product species being monitored, was fit to the appropriate reference spectrum in order to determine the product concentration at the time following the flash corresponding to that scan.

The two spectrometers described above provide complementary experimental information. The single wavelength spectrometer has the advantage of temporal resolution. The minimum

sampling period with this instrument is 10 μ s which is sufficiently short to allow the study of the initial product formation processes involved in this system. However, the sensitivity of the spectrometer is not as high as with other methods of detection, particularly when monitoring ClO. The detection limits for the single wavelength spectrometer are 4×10^{11} molecule cm^{-3} for ClO and 5×10^{10} molecule cm^{-3} for NO_3 . The array spectrometer offers the advantage of higher sensitivity. The multiplex advantage of using up to 1024 channels with the capability of signal averaging for the determination of a single temporal data point provides a tremendous improvement in the signal-to-noise ratio. However, it offers relatively poor temporal resolution, rendering this technique unsuitable for monitoring the nascent photoproducts. Detection limits are more than an order of magnitude less using the diode array spectrometer relative to the single wavelength spectrometer with minimum detectable concentrations of 1×10^{10} molecule cm^{-3} for ClO and 2.5×10^9 molecule cm^{-3} for NO_3 . The somewhat lower sensitivity for ClO is due to the difference in absorption cross sections for ClO and NO_3 ($\sigma_{\text{ClO}} [275.3 \text{ nm}] = 6.7 \times 10^{-18} \text{ cm}^2 \text{ molecule}^{-1}$ vs. $\sigma_{\text{NO}_3} [662 \text{ nm}] = 2.27 \times 10^{-17} \text{ cm}^2 \text{ molecule}^{-1}$) and to the decreased light intensity of the arc lamp which drops by a factor of about two between 662 nm and 275 nm.

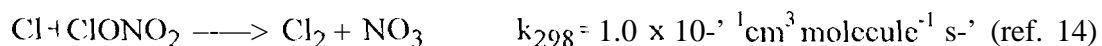
111. Results

Data were collected under a variety of experimental conditions by changing the initial chlorine nitrate concentration, the bath gas identity and density, the photolysis wavelength range, and the temporal resolution of the data acquisition. The experimental conditions for all data collected are summarized in Table 1.

A. NO_3 and ClO Product Yields

Product yields were determined from the ClO and NO_3 signal waveforms. Figure 3 is a plot of a typical NO_3 signal as function of time after photolysis in the Pyrex cell with no additional filtering. Data were acquired with the diode array spectrometer with a time resolution of 16.67 ms. $[\text{ClONO}_2]_0$ was 1.0×10^{14} molecule cm^{-3} with N_2 as the bath gas. Total pressure ranged from 10 - 400 Torr although only the data for 10, 25, 50, and 100 Torr are shown in the figure. Two features of the data are apparent: the maximum NO_3 concentration decreases and the

time required for the NO₃ signal to maximize increases with increasing pressure. NO₃ exhibits secondary formation in this system due to the reaction



However, if it is assumed that the initial chlorine nitrate concentration is constant and the extent of photodissociation does not change, then the rate of secondary NO₃ formation will be independent of pressure. Therefore, the secondary chemistry of this reaction cannot explain the increase in the time to reach the NO₃ maximum observed at higher pressures (see discussion below).

To verify that the observed yield behavior was not a result of the relatively low temporal resolution of the OMA spectrometer, data were also collected using the single wavelength spectrometer with PMT detection. In this case, the temporal resolution of the data was limited only by the 10 μs resolution of the digital oscilloscope. Figure 4 shows data acquired with 50 μs temporal resolution. [ClONO₂]₀ was 2 × 10¹⁴ molecule cm⁻³, and the pressure was varied from 10-50 Torr with N₂ as the bath gas. The same results are observed. The increase in formation time with increasing pressure is particularly evident on this expanded time scale. The first several data points immediately following the flash have been omitted from Figure 4. Although the duration of the xenon flash was only 15 μs, the intensity of the flash in the visible region of the spectrum was so intense relative to the arc lamp that the R955 PMT used for NO₃ detection was saturated by the flash. The recovery period for the PMT was ~200 μs. Accordingly, we were not able to monitor processes occurring at reaction times less than this, but there are no bimolecular processes that can affect the kinetics of NO₃ on this time scale with the reaction conditions employed. These high temporal resolution data confirm the results of the OMA spectrometer measured on a 5 - 20 ms time scale, namely that the decrease in NO₃ yield and the increase in the formation time of the NO₃ signal are a result of the dissociation dynamics of the ClONO₂, and are not caused by secondary chemical processes.

Figures 5 and 6 show signals recorded for the ClO product with the diode array spectrometer and single wavelength spectrometer, respectively. The quality of the signals are not as high as those of NO₃ for the reasons discussed in the experimental section, particularly for the

single wavelength data, but the same general features of decreased yield and increased rise time are present in the ClO data. Of particular importance is the ClO single wavelength data of Figure 6. With the monochromator tuned to 275.2 nm, the R 166U11 PMT does not suffer from the saturation effects seen in the visible region because light from the flash lamp at this wavelength is completely absorbed by the walls of the Pyrex cell. Thus, the ClO temporal behavior can be observed at shorter reaction times. Examination of Figure 6 shows a marked pressure dependence in the ClO yield even on the shortest time scales. Additionally, unlike the NO₃ product, there is no secondary channel for the production of ClO (see the reaction mechanism below), so the observed increase in the formation time of ClO with increasing pressure cannot be due to secondary chemical reactions.

Figure 7 shows typical NO₃ data for photolysis in the quartz cell collected with a temporal resolution of 16.67 ms. For this particular set of data, the initial chlorine nitrate concentration was 1.0×10^{14} molecule cm⁻³, and the pressure was varied from 5 - 400 Torr. There is a pressure dependence exhibited in the NO₃ yield over this pressure range, but the decrease is only a factor of about two, whereas for similar conditions in the Pyrex cell, the yield dropped by more than two orders of magnitude. Also, the temporal behavior of the NO₃ signals observed under these conditions when photolysis is extended to the shorter wavelengths transmitted by the quartz cell is different from the Pyrex data in Figure 3 in that the NO₃ signal maximum occurs immediately following the flash and does not display a secondary formation. Figure 8 shows NO₃ data collected with higher temporal resolution (100 μs) using helium as the bath gas. The observed rise in the NO₃ signal is due solely to reaction 2 and can be fit with a single, first-order rate coefficient. This rise occurs on a time scale much shorter than the temporal resolution of the diode array detector and is therefore not seen in the data of Figure 7. However, the rise of the NO₃ signal observed for photolysis in the quartz cell is independent of pressure and, as expected from reaction 2, the time constant for NO₃ formation changes only as the initial concentration of chlorine nitrate changes.

Figure 9 displays the results of an additional set of measurements taken in the Pyrex cell in which the single wavelength spectrometer was tuned to 225 nm in order to monitor the removal of chlorine nitrate. The initial [ClONO₂] was 1.0×10^{14} molecule cm⁻³, and data were collected

at pressures from 3.2 to 15.1 Torr with N_2 as the bath gas. Because the output of the arc lamp is quite weak at this wavelength, it was necessary to average 300 flashes in order to achieve an acceptable signal-to-noise ratio. The weak signals also limited the pressure range over which meaningful data could be collected. However, the trend in the recorded signals for chlorine nitrate removal is the same as that observed for the NO_3 and ClO product formation, namely, that the magnitude of chlorine nitrate removal decreases with increasing pressure. Although the data are not of sufficient quality over a range of pressures necessary to produce quantitative results, the qualitative features of the data confirm the results obtained when monitoring either the ClO or NO_3 product formation,

Figure 10 shows a comparison of the NO_3 yield collected in the Pyrex cell with the single wavelength and diode array spectrometers. Product yield is defined as the maximum product concentration normalized by the initial chlorine nitrate concentration. Single wavelength data were collected from 3.2 - 50.2 Torr, and diode array data were collected from 3.2 - 400 Torr. All data were normalized to a value of one for the lowest pressure. All data from the two detection schemes result in the same pressure dependence indicating that the observed trends in the yield are not an artifact of one of the detection methods employed. Figure 11 provides a comparison of the NO_3 and ClO product yields. Again, the pressure dependence of the data are very similar—differences in absolute yield are expected due to unequal branching ratios into each product channel. In addition, the similarity in the functional form of the pressure dependences of ClO and NO_3 is an indication that secondary photolysis of the nascent products or secondary chemistry are not creating artifacts which may be mistaken as a pressure dependence. Because the duration of the flash lamp is relatively long and NO_3 absorbs strongly in the visible region of the spectrum, it is possible that the nascent NO_3 product undergoes secondary photodissociation to form $NO + O_2$ and $NO_2 + O$. For ClO the cross sections at wavelengths longer than the 300 nm cut-off of the Pyrex cell are very small, so secondary photodissociation will be insignificant.

The NO_3 yield as a function of air density and photolysis wavelength is shown in Figure 12 with the data presented in Table 11. The four data sets displayed correspond to four different photolysis configurations of the reaction cell, namely, the quartz cell, the Pyrex cell, the Pyrex cell with a chromium potassium sulfate filter, and the Pyrex cell with a ceric ammonium nitrate

filter. Flashlamp spectral distributions for each configuration are shown in Figure 1. The x-axis of Figure 12 covers the range from 0 to about 100 Torr total pressure. The solid lines in the plot are empirical fits to the data and are intended only as a guide to the eye. In each case, the product yield decreases with increasing pressure. In the quartz cell, the decrease is about a factor of two; the data from Pyrex cell photolysis decreases by about 60; the data for the filter solutions decrease by approximately 200 and 350, respectively, for the chromium and ceric solutions. Figure 12 indicates that as the short wavelength cut-off for photolysis is extended to the red, the pressure dependence of the product yield becomes more pronounced.

The inverse NO_3 yield is displayed in Stern-Volmer form in Figure 13 for a series of measurements in which the initial chlorine nitrate concentration and bath gas density were systematically varied. The data are summarized in Table 111. $[\text{ClONO}_2]_0$ ranged from 2.5×10^{13} to 1.0×10^{15} molecule cm^{-3} , and the pressure ranged from 5 to 400 Torr. Included is one set of measurements acquired at a temperature of 220 K. For all chlorine nitrate concentrations, the yield displays a pressure dependence. However, for $[\text{ClONO}_2]_0 \leq 1.0 \times 10^{14}$ molecule cm^{-3} , the functional form of the pressure dependence is independent of the initial chlorine nitrate concentration. For higher $[\text{ClONO}_2]_0$, the drop in the yield with increasing pressure becomes more extreme as the amount of chlorine nitrate is increased. This is indicative of a dissociative mechanism in which self-quenching of the excited electronic state by the parent molecule is important.

11. Product Branching Ratios

The direct measurement of absolute quantum yields was not possible in this experiment, but by measuring both the NO_3 and ClO product yields under identical experimental conditions, it was possible to determine the branching ratios for these two product channels. For these calculations, the branching into the $\text{ClO} + \text{NO}_2$ channel was defined as

$$\beta_{1a} \equiv \frac{[\text{ClO}]_{\text{max}}}{[\text{ClO}]_{\text{max}} + 0.5[\text{NO}_3]_{\text{max}}} = \frac{\Phi_{1a}}{\Phi_{1a} + \Phi_{1b}}$$

where $[\text{ClO}]_{\text{max}}$ and $[\text{NO}_3]_{\text{max}}$ were determined from the maxima of the ClO and NO_3 temporal signals. $\frac{1}{2}[\text{NO}_3]_{\text{max}}$ was used because the $\text{Cl} + \text{NO}_3$ product channel produces two NO_3

molecules due to the fast reaction of Cl with ClONO₂ (reaction 2). It was further assumed that branching into the atomic oxygen channel (reaction 1 c) is negligible relative to the ClO + NO₂ and Cl+NO₃ channels, so that the branching ratio for the Cl+NO₃ channel is given by

$$\beta_{1b} = 1 - \beta_{1a}$$

Branching ratios measured at several values of [ClONO₂]₀ and total pressure are presented in Table IV. Although the absolute product yield for each channel exhibits a pressure dependence, the dependence is the same for both channels, therefore, the resulting branching ratios are pressure-independent. Branching ratios for photolysis in the Pyrex cell are $\beta_{1a} = 0.445 \pm 0.07$ and $\beta_{1b} = 0.56 \pm 0.07$ where the error bounds are reported as 2 σ . When photolysis is extended to shorter wavelengths transmitted by the quartz cell, the branching ratios are $\beta_{1a} = 0.61 \pm 0.06$ and $\beta_{1b} = 0.39 \pm 0.06$.

IV. Discussion

A. Pressure Dependent Product Yields and Formation Rates

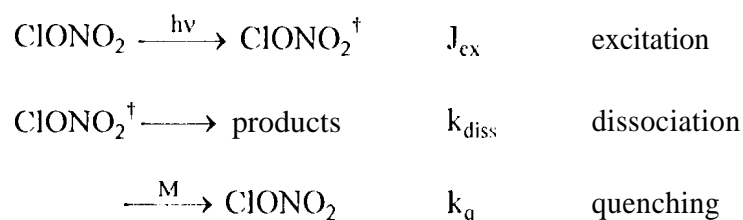
Photodecomposition Mechanism

The pressure dependences of the product yields for NO₃ and ClO formation and ClONO₂ disappearance for photolysis in the Pyrex cell cannot be explained by secondary reactions of the primary products. To establish this we have examined the sensitivity of known secondary processes to changes in the ClONO₂ concentration and buffer gas pressure. The reaction mechanism and rate coefficients for secondary reactions in this system are given in Table V. Because the branching ratio into reaction 1 c is small, the reactions involving atomic oxygen have been neglected in the use of this mechanism for the analysis of the experimental results. The uncertainties in the rate coefficients are greatest for the reactions involving NO₃ with ClO and Cl (reactions 5 and 6); however, these reactions will not have a pressure dependent effect on the product yield--they only affect the rate of product removal.

The simulations produced results in reasonable agreement with the quartz cell data--the differences stem from uncertainties in the rate coefficients for reactions involving NO₃ with Cl and ClO, the reactions of ClONO, and some of the recombination reactions. Simulations

invoking only secondary chemistry, however, fail to replicate the essential feature of the data collected for longer wavelength photolysis, namely, the decrease in product yield and the increase in the formation time with increasing pressure. Simulations of this mechanism over a range of pressures corresponding to the experimental data indicate that the rate of product formation becomes larger at higher pressure with no substantial decrease in the ClO product yield and there is also a small pressure dependence in the NO₃ product yield due to removal by the termolecular combination with NO₂ (reaction 8). This is the intuitively expected result for a mechanism involving termolecular processes. The measured NO₃ time dependence following Pyrex cell photolysis has the opposite behavior, however; the formation time increases and the yield decreases with increasing pressure.

To explain the pressure dependence of the product yield data, it is necessary to invoke a Stern-Volmer-type mechanism in which a metastable electronic state is formed following the initial excitation. This state may dissociate to form products or undergo collisional quenching to the ground electronic state:



This simple mechanism adequately describes the pressure dependence of the product yield, but incorrectly predicts that the rate of product formation becomes faster with increasing bath gas density. This mechanism coupled with the reaction mechanism in Table V can, however, be used to interpret the data collected for photolysis in the quartz cell in which product formation always occurred promptly following the photolysis pulse. The dashed lines in Figure 7 are the resulting fit of this mechanism to the experimental data. The simulated data were produced by simultaneously fitting the measured signals at pressures of 5, 100, and 400 Torr to this Stern-Volmer type mechanism using a least-squares routine (FACSIMILE). Six parameters were varied in the fitting process including $[\text{ClONO}_2]^\dagger$, k_{diss} , and k_q . Three rate coefficients— k_5 , k_6 , and k_x —were also varied in the fitting process in order to allow enough flexibility in the least-squares routine to locate the deepest local minimum on the χ^2 hypersurface. The final values for

these three rate coefficients were within the experimental uncertainty of the accepted values. The rate constants for dissociation and quenching resulting from the fitting routine were $k_d = 1.9 \times 10^7 \text{ s}^{-1}$ and $k_q = 2.6 \times 10^{-12} \text{ cm}^3 \text{ molecule}^{-1} \text{ S}^{-1}$. Whether these values represent a true minimum on the fitting surface is uncertain--varying the initial guesses for each value by a factor of approximately five produced similar numerical results, but we did not perform an exhaustive search of the parameter space of initial values to verify that this was indeed the surface minimum.

It was necessary to modify the above mechanism to include a second long-lived intermediate state (ClONO_2^\ddagger) to more closely approximate the NO_3 yield and temporal behavior for photolysis in the Pyrex cell, *i.e.*,

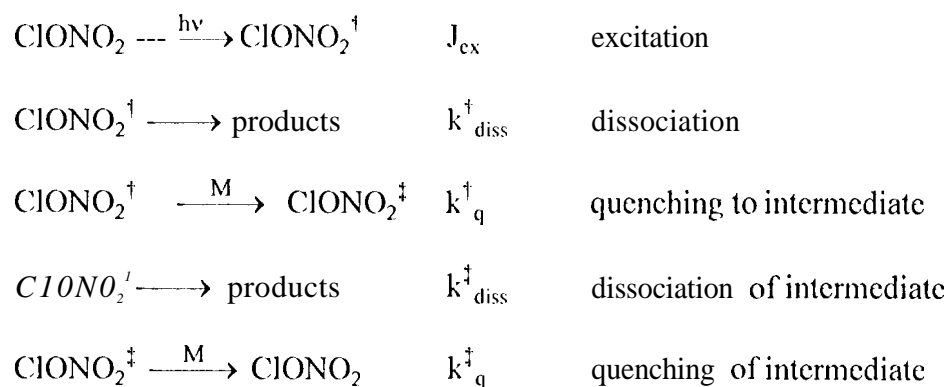


Figure 14 shows simulations of the NO_3 temporal signals of Figure 3 using the modified mechanism which also includes the secondary reactions given in Table V. The simulations qualitatively describe the essential features of the data, namely, a decrease in yield and an increase in product formation time with increasing bath gas density. It was not possible, however, to obtain a robust fit to observed NO_3 temporal profiles over the entire pressure range. One reason for this may be the complexity introduced by using a broadband flash lamp as a photolysis source. Under our experimental conditions, the initial absorption step prepares a large ensemble of excited states possibly in different electronic levels. The interactions between these states is not well understood, and it is therefore difficult to quantify the effects. In addition, the modified mechanism may not be a complete description of the dynamics of chlorine nitrate photolysis under our experimental conditions. In measurements performed using a ferric chloride solution in the filter jacket, the short wavelength cut-off was extended to approximately

400 nm limiting the excitation to only the very weakest transitions in the absorption spectrum. The NO_3 product exhibited two distinct maxima separated in time by about 1.0 sec. This may be an indication of multiple intermediates involved in the dissociation.

Recent *ab initio* calculations by Graña *et al.*¹⁰ determined the vertical excitation energies for transitions from the chlorine nitrate ground state to excited electronic states in the singlet and triplet manifolds. They also determined oscillator strengths for the singlet→singlet transitions and used these results to interpret the chlorine nitrate uv-visible absorption spectrum. They assigned the large feature centered at 190 nm to the $1^1A' \rightarrow 4^1A'$ transition ($\pi \rightarrow \pi^*$ excitation) and the peak at 215 nm to the $1^1A' \rightarrow 3^1A''$ transition ($n \rightarrow \pi^*$ excitation). The weak absorption band at 370 nm was not assigned because it lies approximately 1 eV below the lowest calculated excited singlet state. The temperature dependence of the absorption spectrum measured by Burkholder *et al.*¹⁶ suggests that this low energy band derives from a transition from the ground electronic state. The bands at 215 nm and 370 nm were the only absorption features that were not reduced in relative intensity with decreasing temperature. It is likely that the 370 nm band arises from a spin forbidden transition from the ground state to the lowest lying triplet state. The position of this band corresponds very well with the vertical excitation energy calculated by Graña *et al.* for this process, and the small cross section indicates that the transition is forbidden.

With the information provided by the *ab initio* results of Graña *et al.*, the electronic states involved in the mechanism for the broadband photolysis of chlorine nitrate can be tentatively assigned. An energy diagram of the excited chlorine nitrate states is shown in Figure 15. Photolysis in the unfiltered quartz cell is dominated by excitation to the $3^1A''$ state which rapidly dissociates to products. Photolysis in the unfiltered Pyrex cell with a short wavelength cut-off at 300 nm restricts the number of excited states that are energetically accessible. The uncertainty in the calculated vertical excitation energies is -0.2 eV. The $1^1A''$ state is accessible in our experiments if the calculated energy of this state is over-estimated by 0.23 eV which is consistent with the stated uncertainties of the computational results. The only other states energetically accessible are in the triplet manifold with the $1^3A''$ state clearly within the energy range of the photolyzing light, and the $1^3A'$ state perhaps accessible if the calculated energy is high by 0.17 eV. As stated above, in order to qualitatively simulate the data, it was necessary to

invoke the participation of two excited electronic states. Therefore, we believe that the initial excitation is dominated by the transition to the $1^1A''$ state with possibly some population going into the triplet manifold. The $1^1A''$ state undergoes competition between dissociation to products and intersystem crossing to the triplet manifold. From their calculations and by analogy to nitric acid, Graña *et al.* determined that the lowest lying triplet state is metastable in that the $1^3A''$ state represents a local minimum on the potential energy surface. Because the $1^3A''$ state is metastable, it is expected to have a long lifetime relative to dissociation to products or collisional quenching to the ground electronic state. Population of this state is likely to occur by through a rapid spin-orbit radiationless transition which is known to be rapid in systems involving heavy atoms such as chlorine. This is consistent with our observation that photolysis of chlorine nitrate at longer wavelengths proceed via a mechanism that involves a long-lived intermediate state,

Metastable Intermediate Detection

We have shown recently that the broadband photolysis of dichloride monoxide (Cl_2O) at wavelengths beyond the Pyrex cutoff (300 nm) results in pressure-dependent ClO quantum yields.¹⁷ The similarities between ClONO_2 and Cl_2O are striking in that both molecules exhibit a decrease in the product yield and a decrease in the rate of product formation for an increase in the total pressure. The analysis for Cl_2O is simpler because of the less complicated secondary chemistry of the products (ClO and Cl). In our Cl_2O study, a transient absorption spectrum was detected following Cl_2O photolysis in the Pyrex cell. Vibrational progressions were identified in this spectrum which were consistent with the transient species being Cl_2O . *Ab initio* calculations of band oscillator strengths in the singlet and triplet manifolds suggested that the observed spectrum could be assigned to a very intense $2^3A_2 \leftarrow 1^3B_1$ transition. This implied that a radiationless transition to the triplet manifold in Cl_2O is rapid, and that the resulting triplet states are sufficiently long-lived to undergo collisional relaxation, causing the observed pressure-dependent quantum yields.

For the chlorine nitrate photolysis experiments, we attempted to identify spectroscopic evidence for the existence of metastable states, but for a number of reasons we were unable to observe any transient absorption spectra in the 250-600 nm spectral range. For example, the

oscillator strengths for excitations from the intermediate state to higher energy triplet states may be very small. In the case of Cl_2O , the transition from the lowest energy triplet state, 1^3B_1 , to the 2^3A_2 state has a calculated oscillator strength greater than 0.1. Unfortunately, the *ab initio* techniques employed by Graña *et al.* did not allow for the computation of oscillator strengths in the triplet manifold. Another reason for the lack of experimental evidence of the intermediate state is that its lifetime may be short relative to the 170 ms temporal resolution of the detection scheme used to search for the metastable absorption spectrum. Finally, spectral interferences from ClONO_2 , ClO or NO_3 may have complicated the search.

B. Possible Experimental Artifacts

The possibility that the observed pressure dependence of the photolysis product yield was caused by experimental artifacts was thoroughly investigated. The first, and perhaps most obvious, artifact would be wall processes in which dissociation occurs at the cell walls, and the temporal dependence of the signals is determined by diffusion back into the viewing region. As the pressure in the cell increases, the time required to diffuse to the walls and back into the viewing region of the arc lamp would increase, thus explaining the increased formation time of the product signals. However, if reactions at the cell walls were responsible for the formation of product, similar behavior should be observed independent of the cell material (quartz vs. Pyrex) and of the salt solution in the filter jacket (no filtering vs. ceric ammonium nitrate vs. chromium potassium sulfate filters). Each of these experimental configurations displayed marked differences in the observed signals, thus arguing against wall processes. Additionally, measurements were made in the Pyrex cell under identical conditions of chlorine nitrate concentration and bath gas pressure using a number of different bath gases. For the cases in which either N_2 or O_2 were used, the diffusion rate through the cell is approximately equal due to the similarities in molecular weight and size, so the loss from wall effects would be expected to be similar. However, a comparison of the signals shows that the product formation time approximately doubles when changing the bath gas from O_2 to N_2 . This is additional evidence against a diffusion controlled process such as wall reactions.

Another possible artifact would be dark dissociative processes, *i.e.*, the high voltage discharge of the flash lamp creates a plasma not only in the xenon jacket, but also within the

reaction cell itself which results in the dissociation of chlorine nitrate from a mechanism not associated with the absorption of light. Such a plasma would be highly dependent on the total pressure in the cell and might produce the observed effect in the product yields. Again, the difference between the cell configurations argues against such a mechanism in that seemingly small changes in cell properties (quartz to Pyrex) which have no effect on the xenon discharge result in dramatic changes in the product behavior. To provide further evidence against such an artifact, a set of measurements were carried out in which, first, the NO_3 product yield was determined at a number of pressures in the quartz cell with no other filtering of the photolysis wavelengths. Then a tube of thin Pyrex glass of the same length as the inner reaction cell was inserted into the quartz cell, and the measurements were repeated. The quartz cell data displayed the same small pressure dependence seen in Figure 12, but by inserting the Pyrex tube, the yield decreases with pressure as observed in the Pyrex cell. "Thus, the quartz cell can be "converted" into the Pyrex cell without changing the physical properties of the discharge.

Another possible explanation for the observed pressure dependent yields is the existence of a very efficient chain mechanism which catalyzes the decomposition of ClONO_2 and is initiated by the photolysis flash and quenched with increasing pressure. Such a catalytic mechanism is unlikely as atomic chlorine is the only known chain carrier which reacts rapidly with ClONO_2 , and this reaction terminates the chain..

C. Comparison with Previous Work

Branching Ratios

A number of studies have examined the photolysis of chlorine nitrate¹⁻⁹ with several being of particular relevance to the current work. Margitan measured the product channel branching ratios following photolysis at 266 nm and 354 nm using an atomic fluorescence technique to detect the atomic chlorine product and chemical conversion to detect ClO by reaction with NO to form Cl.⁶ He reported quantum yields of $\Phi_{1b} = 0.90 \pm 0.10$ and $\Phi_{1c} = 0.10 \pm 0.10$ and saw no evidence for the ClO product. Marinelli and Johnston detected the NO_3 product at 662 nm using absorption spectroscopy following 248 nm photolysis.⁵ They reported a quantum yield of 0.55 (+0.3/-0.1) for channel 1b. Minton *et al.* used a molecular beam apparatus to measure the Cl, ClO, and NO_2 products by time- and angle- resolved mass spectrometry following photolysis at

193 nm and 248 nm.⁸ They reported quantum yields of $\Phi_{1a} = 0.36 \pm 0.08$ and $\Phi_{1b} = 0.645 \pm 0.08$ for 193 nm photolysis and $\Phi_{1a} = 0.46 \pm 0.08$ and $\Phi_{1b} = 0.54 \pm 0.08$ for 248 nm photolysis. They found no evidence for channel 1c and placed an upper limit on the branching into this channel of 0.04. These results have recently been extended to 308 nm by Moore *et al.*¹⁹ who obtained $\Phi_{1a} = 0.33 \pm 0.06$ and $\Phi_{1b} = 0.67 \pm 0.06$. The quantum yields of Marinelli and Johnston, Minton *et al.*, and our results presented in Table IV are in reasonable agreement. The results reported by Margitan lie well outside the error bounds of these three studies, but a careful examination of Margitan's work fails to reveal a clear reason for the discrepancy. Recent unpublished results by Burkholder and co-workers²⁰ at wavelengths between 193 nm and 351 nm, and Orlando and co-workers²¹ at 248 nm and 308 nm confirm that there is a substantial yield of ClO for ClONO₂ photolysis over the range 193-308 nm.

The small difference in branching ratios between our measurements performed in the quartz cell and the quantum yield results of Minton *et al.* for 193 nm photolysis may stem from the electronic states excited in the initial absorption step. Photolysis at 193 nm is dominated by a $\pi \rightarrow \pi^*$ transition ($1^1A' \rightarrow 4^1A'$) localized on the NO₂ moiety whereas quartz cell photolysis is dominated by a $n \rightarrow \pi^*$ transition ($1^1A' \rightarrow 3^1A''$) also localized on the NO₂ moiety.¹⁰ The intramolecular couplings will be different for each case with the $n \rightarrow \pi^*$ transition favoring dissociation of the weaker O-N bond ($\Delta H^\circ = 109 \text{ kJ mol}^{-1}$), and the $\pi \rightarrow \pi^*$ transition favoring dissociation of the Cl-O bond ($\Delta H^\circ = 167 \text{ kJ mol}^{-1}$).

Buffer Gas Quenching

The lifetimes of intermediate states and the dependences of product yields on buffer gas pressure in ClONO₂ photolysis have not been systematically studied until recently. The molecular beam photodissociation experiments of Okumura, Minton and co-workers provide information concerning the lifetimes of possible intermediate states.^{8,19} In these experiments, angular distributions were measured by electron-impact mass spectroscopy in the recoil of ClONO₂ photodissociation products at 193, 248 and 308 nm. At all three wavelengths, the observed products were scattered anisotropically indicating that the lifetimes of the dissociating states were less than a rotational period. Recent work by Burkholder *et al.*²⁰ found no pressure dependences for photolysis at 193, 248, 308 or 351 nm although at the latter wavelength, the

extremely small chlorine nitrate absorption cross sections and impurities were significant complications, 308 nm is very near the cutoff of the Pyrex flash photolysis cell used in these experiments. The results of Okumura *et al.* and Burkholder *et al.* at this wavelength which imply prompt dissociation are therefore not incompatible with our results obtained using the Pyrex cell. Our results appear to be inconsistent with the 351 nm results of Burkholder *et al.*, however. The main difference in experimental technique is the use of a broadband photolysis source in our experiments. Whether the excitation of an ensemble of states using broadband photolysis plays a significant role in the dissociation dynamics is uncertain, but may be one source for the differences in observed product yields.

ClONO₂ Self-Quenching

A modified Stern-Volmer mechanism provides a reasonable explanation for the effect of the initial chlorine nitrate concentration on the pressure dependence of the quantum yield as shown in Figure 13. The quenching efficiency for excited electronic states will be much greater for chlorine nitrate than for the buffer gas because of the exact overlap of energy levels and the increased number of vibrational modes in ClONO₂. At low [ClONO₂], the collisional frequency between excited and ground state chlorine nitrate is so small that the enhanced quenching efficiency has no observable effect relative to quenching by the bath gas, whereas at higher [ClONO₂], the collisional frequency increases and self quenching becomes significant as illustrated in Figure 13.

Burrows *et al.* observed dependences of the quantum yields for NO₃ formation and ClONO₂ removal on the [ClONO₂]₀ in the steady-state photolysis of ClONO₂ at 254 nm. To explain these results, they invoked a mechanism involving a metastable chlorine nitrate intermediate which could undergo either dissociation to products or efficient self-quenching back to the ground state. While the mechanism we have proposed to explain the observed product yields from photodissociation is similar to that of Burrows *et al.*, our mechanism is applicable only at wavelengths longer than 300 nm. The Burrows *et al.* results imply a lifetime for the excited state that is longer than about 10⁻⁴ s because their observed quantum yields decrease for [ClONO₂] > ~ 10¹⁴ molecule cm⁻³. This is inconsistent with the results of Okumura *et al.*⁸ which

give an excited state lifetime less than 10^{-7} s at for 248 nm photoexcitation. Burrows *et al.* did not examine the effects of buffer gas quenching in their studies.

Pressure dependent photolysis quantum yields have been observed in a number of gas phase studies involving other molecules. Early work by Ayscough and Steacie on the photolysis of hexafluoroacetone at 313 nm revealed a dependence of both the CO and C_2F_6 quantum yields on the hexafluoroacetone pressure.²² Their data were well explained with a classic Stern-Volmer mechanism with a decomposition to deactivation ratio of 1:60. In the steady state photolysis of thiophosgene ($SCCl_2$), Okabe also reported pressure effects in the chlorine atom quantum yield. For photolysis at wavelengths of 253.7 nm and shorter, the chlorine atom exhibited unity quantum yield, but when photolysis occurred at 366.0 nm or 435.8 nm, the quantum yield had a pressure dependence which could be well fit with a simple Stern-Volmer mechanism. Additionally, the magnitude of the effect varied from 366.0 nm to 435.8 nm with the pressure dependence most pronounced at the longer wavelength.

1). Atmospheric implications

The implications of these results for the partitioning of inorganic chlorine, in the lower stratosphere are potentially significant. The product of solar flux and $ClONO_2$ cross section maximizes at about 330 nm in the lower stratosphere. Reduction of the photodissociation quantum yields due to collision effects would be especially important for excitation in the 290-450 spectral region and would result in an underprediction of the ratio $[ClONO_2]/[HCl]$ by atmospheric models. This will cause the models to overestimate the rate of ozone catalytic destruction by the chain mechanism which involves $ClONO_2$ photolysis.²⁴

Atmospheric models estimate J-values in each altitude bin by performing a wavelength integration on the product of absorption cross section, dissociation quantum yield and solar flux. Due to the broadband nature of the photolysis pulse from the flash lamp, it is not possible to retrieve wavelength dependent quantum yields from this experiment for use in model calculations. Some qualitative observations can be made, however. The wavelength distribution of the photolysis radiation from the Pyrex cell mimics the solar spectral distribution because both spectral distributions cut off at about 300 nm. As shown in Fig. 10, a direct application of the

results of the Pyrex cell experiments would therefore imply a reduction in J_{ClONO_2} of about a factor of ten relative to the low-pressure limiting case at an altitude of 20 km. This is very likely to be an overestimate of the effect in the atmosphere, however because the solar spectrum extends to somewhat shorter wavelengths and the solar flux increases more rapidly with wavelength than the Pyrex flash lamp spectrum. These factors increase the weighting of solar photolysis to shorter wavelengths than our experiment which will reduce the sensitivity of the photolysis rate toward molecular collisions. A more precise determination will require the measurement of the pressure dependence of the quantum yield at several discrete wavelengths throughout the 290-450 nm spectral region.

Since present stratospheric models do not consider the effect of pressure on the $\text{ClONO}_2/\text{HCl}$ values, we would expect that these models would tend to overpredict HCl and underpredict ClONO_2 mixing ratios in the lower stratosphere. There are relatively few simultaneous direct measurements of the partitioning of inorganic chlorine in the lower stratosphere with which to validate the models. The most rigorous test of photochemical models comes from instruments on balloons, satellites and aircraft which directly measure vertical profiles of ClONO_2 , HCl and other species such as O_3 which have a strong influence on chlorine partitioning. One such data set is provided by the Mark IV balloon solar interferometer of Toon and co-workers. This instrument records infrared atmospheric spectra at sunset and sunrise during flights from a float altitude of 40 km. near Ft. Sumner, NM.²⁵ These spectra are inverted to provide vertical concentration profiles of ClONO_2 , HCl and many other species from the tropopause (12 km.) to 40 km. Jaeglé *et al.* have compared measurements from balloon flights from 1990-1993 with results from the Caltech-JPL one-dimensional atmospheric model using kinetic and photochemical parameters recommended by DeMore *et al.*. In particular, they found that their model underpredicted the $[\text{ClONO}_2]/[\text{HCl}]$ measurements of Toon *et al.* below 20 km. At these altitudes, where the collisional quenching of ClONO_2 metastable states would be expected to play a role, it was found that the agreement would be improved if values of J_{ClONO_2} were reduced from their nominal values by a factor varying from 1 to 10 as the altitude decreased from 20 to 12 km. Data sets from other atmospheric instruments are consistent with this conclusion. Recently, Dessler *et al.* have shown that standard chemistry underpredicts $[\text{ClONO}_2]/[\text{HCl}]$

compared with global data at 20 km. from the Upper Atmosphere Research Satellite²⁶. Also, midlatitude *in situ* measurements of [11(1)] from the ER-2 aircraft between 15 and 20 km. by Webster *et al.*²⁷ are significantly smaller than model predictions however there are no simultaneous measurements of [ClONO₂] with which to define the partitioning of inorganic chlorine.

There are other atmospheric measurements which do not support a pressure dependence in J_{ClONO_2} . Michelson *et al.* find reasonably good agreement between their 1-D model and ATMOS measurements of [~1C]NO₂/[11~1] in the lower stratosphere using pressure-independent ClONO₂ quantum yields.²⁸ Also, *in situ* measurements of [ClO] between 15 and 20 km. from the ER-2 aircraft²⁹ and from balloons³⁰ tend to be larger than predicted by standard models whereas a decrease in J_{ClONO_2} that would be consistent with the measurements of Leeson *et al.* would result in a slight reduction in [ClO]. There are also a number of other possible explanations for deviations between the observed inorganic chlorine partitioning and model predictions including heterogeneous reactions on volcanic aerosols, missing reservoir(s) of inorganic chlorine and measurement errors. Remote sensors are currently the only instruments capable of direct ClONO₂ measurements. Because most of the HCl and ClONO₂ column density lies above 20 km, retrievals below this altitude are subject to large uncertainties,

V. Summary

The broadband photolysis of chlorine nitrate has been studied in both the strongly allowed and weak tail regions of the absorption spectrum. Time-resolved long-path absorption spectroscopy has shown that both the Cl+NO₃ and ClO+NO₂ product channels are active. There is strong evidence for dependences of the quantum yields for product formation and ClONO₂ disappearance on the ClONO₂ and buffer gas densities. The functional form of the product yield vs. bath gas density is strongly dependent on the spectral distribution of the flash lamp. As the photolyzing light is limited to wavelengths longer than 300 nm, the product yield decreases more rapidly with increasing bath gas density. These results imply that, following excitation beyond ~ 320 nm, ClONO₂ undergoes a radiationless transition to a long-lived metastable electronic state induced by strong spin-orbit coupling. Comparison with *ab initio*

results suggest that the metastable species is the lowest energy triplet state, $1^3A''$. These observations are consistent with a mechanism we have proposed recently for the photodissociation of Cl_2O . In the latter study, broadband photolysis beyond 300 nm gives rise to a metastable triplet state which is observable by UV absorption spectroscopy.

The branching ratios into the $\text{ClO} + \text{NO}_2$ and $\text{Cl} + \text{NO}_3$ channels have been measured under two different experimental spectral regions. For photolysis in the unfiltered Pyrex cell ($\lambda > 300$ nm), the results are $\beta_{\text{ClO}} = 0.44 \pm 0.07$ and $\beta_{\text{NO}_3} = 0.56 \pm 0.07$. These results are in excellent agreement with two other studies of the chlorine nitrate branching ratios.^{5,8} For photolysis in the unfiltered quartz cell ($\lambda > 200$ nm), the branching ratios are $\beta_{\text{ClO}} = 0.61 \pm 0.06$ and $\beta_{\text{NO}_3} = 0.31 \pm 0.06$.

The observed quantum yield pressure dependence beyond 300 nm has implications for the partitioning of inorganic chlorine in the stratosphere between the tropopause and 20 km. Although there are major uncertainties in both models and atmospheric field measurements, comparisons between predicted and observed concentrations of HCl and ClONO_2 in this altitude region seem to be improved if the models employed pressure-dependent ClONO_2 quantum yields. Further laboratory measurements and future *in situ* observations of ClONO_2 , HCl and ClO will help to better quantify the role of pressure dependence in the photolysis of ClONO_2 and possibly other species.

VI. Acknowledgment

We thank the JPL Kinetics and Photochemistry Group, R. Salawitch, C. Webster, Y. Yung, L. Jaeglé, M. Okumura, T. Minton and T. Moore for many valuable discussions and preprints of their work. This research was performed by the Jet Propulsion Laboratory, California Institute of Technology, under contract with the National Aeronautics and Space Administration.

References

1. Smith, W.S.; Chou, C.C.; Rowland, F.S. *Geophys. Res. Lett.* 1977, 4, 517.
2. Chang, J. S.; Barker, J.R.; Davenport, J.E.; Golden, D.M. *Chem. Phys. Lett.* 1979, 60, 385.
3. Adler-Golden, S. M.; Wiesenfeld, J.R. *Chem. Phys. Lett.* 1981, 82, 281.
4. Knauth, K.D.; Schindler, R.N. *Z. Naturforsch.* **1982**, 38a, 893.
5. Marinelli, W. J.; Johnston, H.S. *Chem. Phys. Lett.* 1982, 93, 127.
6. Margitan, J.J. *J. Phys. Chem.* 1983, 87, 674.
7. Burrows, J. P.; Tyndall, G. S.; Moortgart, G.K. *J. Phys. Chem.* 1988, 92, 4340.
8. Minton, 'T. K.; Nelson, C.M.; Moore, 'T. A.; Okumura, M, *Science* 1992, 258, 1342; Nelson, C.M.; Moore, R. A.; Okumura, M.; Minton, 'T. K.; submitted to *Chem. Phys.*
9. De Saxce, A.; Schriver, I., *Chem. Phys. Lett.* 1992, 199, 596,
10. Graña, A. M.; Lee, 'T. J.; Head-Gordon, M. *J. Phys. Chem.* 1995, 99, 3493.
11. Sander, S.P.; Friedl, R.R. *J. Phys. Chem.* **1989**, 93, 4764.
12. Cady, G.H. *Inorg. Syn.* 1967, 5, 156.
13. Sander, S.P. *J. Phys. Chem.* **1986**, 90, 4135.
14. DeMore, W.B.; Sander, S.P.; Golden, D.M.; Hampson, R.F.; Kurylo, M. J.; Howard, C. J.; Ravishankara, A.R.; Kolb, (S. J.) {.; Molina, M.J. *Chemical Kinetics and Photochemical Data for Use in Stratospheric Modeling--Evaluation Number 11* JPL Publication 94-26, Jet Propulsion Laboratory, California Institute of Technology, Pasadena, CA.
15. Nickolaisen, S.I.; Friedl, R.; Sander, S.P. *J. Phys. Chem.* **1994**, 98, 155.
16. Burkholder, J.B.; Talukdar, R. K.; Ravishankara, A.R. *Geophys. Res. Lett.*, 1994, 21, 585.
17. Nickolaisen, S.I.; Miller, C.E.; Sander, S.P.; Hand, M.R.; Williams, I.H.; Francisco, J.S. *J. Chin. Phys.* submitted.
18. Okabe, H. *Photochemistry of Small Molecules* John Wiley & Sons, New York, 1978,
19. Moore, 'T. A.; Okumura, M.; Tagawa, M.; Minton, T.K.. *Faraday Discuss.* 1995, 100, xxx.
20. Burkholder, J.B. *et al.*, paper presented at the American Chemical Society Meeting, Chicago, IL, 1995
21. Orlando, J.J. Keglcy-Owen, C. S., Tyndall, G.S. and Calvert, J. G., Proceedings of the XXIst Informal Conference on Photochemistry, Toronto, Ontario, Canada, May, 1994.
22. Ayscough, P.B.; Steacie, E.W.R. *Proc. Royal Soc., A* 1956, 234, 476.
23. Okabe, I. *J. Chem. Phys.* 1977, 66, 2058.

- 24, papers on clono2 photolysis including Toumi (ask ross)
25. Jacglé, I.; Toon, G. *Manuscript in preparation*.
26. Dessler, A.E.; Considine, D.B.; Morris, B. A.; Schoeberl, M.R.; Russell 111, J. M.; Roche, A.E.; Kumer, J.B.; Mergenthaler, J.J.; Waters, J. W.; Gille, J.C. and Yuc, G. K.; *Geophys. Res. Lett.*, 1998, 22, 1721.
27. Webster, C.R.; *Geophys. Res. Lett.*, 1994, 21, 2575.
28. Michelsen, H.A. *et al.*, submitted to *Geophys. Res. Lett.*
29. Stimpfle, R.M. *et al.*, *Geophys. Res. Lett.*, 1994, 21, 2543.
30. Avallone, L.M. *et al.*, *Geophys. Res. Lett.*, 1993, 20, 1795,

Table I. Summary of experimental conditions,

Species detected	[ClONO ₂] (molecule cm ⁻³)	Bath Gas	Pressure (Torr)	Detection ^a Scheme	Cell	Number of runs
ClO	1.2- 3.2	He	3.9-75	OMA	Pyrex	19
NO ₃	0.5 -3.3	He	3.9-600	OMA	Pyrex	42
NO ₃	1.6- 8.1	He	10-75	PMT	Pyrex	51
ClO	1.3 -8.0	He	5.4-75	PMT	quartz	23
NO ₃	1.3 -6.5	He	5.4-75	PMT	quartz,	40
NO ₃	1.8 -8.0	He	10-75	PMT	quartz/NiSO ₄ ^b	11
ClONO ₂	3.2	He	10-75	PMT	quartz	4
ClO	0.51 -1.0	N ₂	5.0-50	OMA	Pyrex	15
ClO	2.0	N ₂	13-25	PMT	Pyrex	4
NO ₃	0.25-10	N ₂	3.0-400	OMA	Pyrex	110
NO ₃	2.0- 4.0	N ₂	6.4-50	PMT	Pyrex	18
NO ₃	0.25-10	N ₂	5.0 -400	OMA	quartz	71
NO ₃	1.0	N ₂	5.0 -400	OMA	Pyrex/Ni,G~	8
NO ₃	1.0	N ₂	5.0- 100	OMA	Pyrex/KMnO ₄ ^d	5
NO ₃	1.0	N ₂	3.2-25	OMA	quartz/FeCl ₃ ^e	9
NO ₃	1.0	N ₂	3.2-50	OMA	Pyrex/ccricf	7
ClONO ₂	1.0	N ₂	3.2-20	PMT	Pyrex	6
ClONO ₂	1.0	N ₂	3.2- 100	PMT	quartz	11
ClONO ₂	1.0	N ₂	3.1-25	PMT	quartz/FeCl ₃ ^e	11
NO ₃	0.75 -1.0	O ₂	5.0-200	OMA	Pyrex	17
NO ₃	2.0	O ₂	10-50	PMT	Pyrex	4
NO ₃	0.50 -2.5	air	3.0-250	OMA	Pyrex	43
NO ₃	0.75 -4.0	air	2.4-400	OMA	quartz	49
NO ₃	0.75 -2.0	air	3.2-100	Oh4A	Pyrex/ccricf	21
NO ₃	1.0 -5.0	air	3.2- 100	OMA	Pyrex/ CrK(SO ₄) ₂ ^g	19

a) OMA = optical multi-channel diode array spectrometer; PMT = photomultiplier tube single wavelength spectrometer,

b) Filter solution made of 500 g l⁻¹ NiSO₄•6H₂O in water.

c) Filter solution made of 500 g l⁻¹ NiSO₄•6H₂O and 300 g l⁻¹ CoSO₄•7H₂O in water,

d) Filter solution made of 0.25 g l⁻¹ KMnO₄ in water.

e) Filter solution made of 1.0 g l⁻¹ FeCl₃ in water.

f) Filter solution made of 5.0 g l⁻¹ (N114)2C:c@'03)6 in water.

g) Filter solution made of 50 g l⁻¹ CrK(SO₄)₂•12H₂O in water.

Table 11. NO₃ yields for quartz cell, Pyrex cell, Pyrex cell with chromium potassium sulfate filter, and Pyrex cell with eerie ammonium nitrate filter. Chlorine nitrate concentration for all data presented was 1.0 x10¹⁴ molecule cm⁻³.

Cell configuration	Air density (10 ¹⁸ molecule cm ⁻³)	[NO ₃] _{max} (10 ¹² molecule cm ⁻³)	standard deviation (10 ¹² molecule cm ⁻³)
quartz	0.000	4.699	0.0073
	0,000	6.050	0.0040
	0.057	5.680	0.0037
	0.084	3.842	0.0118
	0,224	4.384	0.0046
	0.242	2.980	0.0079
	0.389	3.867	0.0038
	0.409	2.584	0.0095
	0.713	3.559	0.0051
	0.737	2.441	0.0096
	1.515	3.518	0.0063
	1.549	2.411	0.0087
	3.138	3.164	0.0083
	3.161	2.176	0.0103
Pyrex	0.000	1.047	0.0050
	0.021	0.817	0.0053
	0.046	0.598	0.0134
	0.062	1.092	0.0061
	0.086	1.007	0.0070
	0.115	0.651	0.0069
	0.224	0.567	0.0067
	0.253	0.480	0.0048
	0.273	0.385	0.0089
	0.386	0.272	0.0056
	0.412	0.165	0.0065
	0.435	0.190	0.0069
	0.707	0.109	0.0061
	0.734	0.0808	0.0058
	0.762	0.0822	0.0083
	1,522	0.0425	0.0053
	1.543	0.0429	0.0074
	1.575	0.0227	0,0055
	3.143	0.0253	0.0033
	3.164	0.0207	0.0077
	3.241	0.0184	0.0058
	6.387	0.0232	0.0043

Table 11. (con't.)

Cell configuration	Air density (1 0 ¹⁸ molecule cm ⁻³)	[NO ₃] _{max} (1 0 ¹² molecule cm ⁻³)	standard deviation (1 0 ¹² molecule cm ⁻³)
Pyrex/ CrK(SO ₄) ₂ •12H ₂ O	0.039	2.810	0.0098
	0.057	0.312	0.0030
	0.063	0.374	0.0076
	0.089	0.404	0.0043
	0.119	0.170	0.0058
	0.139	0.0981	0.0022
	0.166	0.135	0.0055
	0.222	0.0883	0.0046
	0.223	0.0541	0.0056
	0.248	0.0493	0.0047
	0.283	0.0340	0.0067
	0.386	0.0485	0.0029
	0.386	0.0220	0.0032
	0.412	0.0191	0.0078
	0.605	0.0276	0.0059
	0.706	0.0168	0.0049
	0.713	0.0184	0.0043
	0.734	0.0140	0.0054
	1.419	0.0074	0.0050
	3.039	0.0064	0.0018
Pyrex/ (NH ₄) ₂ Ce(NO ₃) ₆ filter	3.139	0.0057	0.0018
	0.000	0.0064	0.0037
	0.056	3.677	0.0050
	0.072	0.445	0.0069
	0.090	0.187	0.0057
	0.142	0.124	0.0038
	0.173	0.119	0.0075
	0.224	0.0764	0.0033
	0.236	0.0564	0.0109
	0.340	0.111	0.0056
	0.383	0.0497	0.0024
	0.564	0.0383	0.0028
	0.653	0.108	0.0061
	0.715	0.0361	0.0019
	1.361	0.0255	0.0047
	1.471	0.0417	0.0045
	1.517	0.0210	0.0017
	2.992	0.0180	0.0040
	3.081	0.0378	0.0092
	3.148	0.0127	0.0027
		0.0174	0.0025

Table III. Inverse NO_3 yield, ϕ_{NO_3} , as a function of initial chlorine nitrate concentration and N_2 bath gas density for photolysis in the Pyrex. ϕ_{NO_3} is defined as $[\text{ClONO}_2]_0/[\text{NO}_3]_{\text{max}}$.

$[\text{ClONO}_2]_0$ (10^{14} molecule cm^{-3})	N_2 density (10^{18} molecule cm^{-3})	ϕ_{NO_3}	Temperature (K)
0.25	0.073	24.0	298
	0.137	28.6	
	0.217	33.8	
	0.299	39.2	
	0.794	168.0	
	1.608	306.5	
	2.417	489.6	
	3.215	958.7	
0.50	0.046	21.6	298
	0.112	23.4	
	0.193	29.5	
	0.273	35.2	
	0.438	88.7	
	0.597	132.1	
	0.765	157.4	
	1.579	385.8	
	2.396	614.4	
	3.192	679.8	
	6.440	1313.	
	9.693	1779.	
0.75	12.92	2660.	298
	0.164	28.0	
	0.248	24.2	
	0.407	55.1	
	0.575	137.6	
	0.733	138.0	
	1.544	325.8	
	2.366	539.0	
	3.168	694.4	
	6.409	440.	
	9.655	2284.	
	12.89	2918.	

Table III. (con't.)

$[C10NO_2]_0$ (10 ¹⁴ molecule cm ⁻³)	N ₂ density (10 ¹⁸ molecule cm ⁻³)	ϕ_{NO_3}	Temperature (K)
1.00	0.148	47.1	220
	0.365	54.4	
	0.585	132.2	
	1.017	233.6	
	2.154	538.6	
	3.233	777.6	
	4.333	1066.	
	0.230	35.8	298
	0.714	179.4	
	1.522	456.4	
	2.342	748.5	
	3.137	980.4	
	6.387	1828.	
	9.626	2990.	
	12.86	3321.	
2.00	0.120	35.8	298
	0.608	199.2	
	1.423	586.3	
	2.230	992.6	
	3.041	300.	
	6.251	422.	
	9.525	393.	
	2.76	400.	
3.00	0.181	51.2	98
	0.512	250.2	
	1.313	748.7	
	2.128	226.	
	2.948	630.	
	6.185	703.	
	9.420	206.	
	12.66	479.	
4.00	0.080	65.5	98
	0.407	139.0	
	0.486	280.0	
	1.218	953.5	
	2.039	1538.	
	2.843	866.	
	6.075	2719.	
	9.320	3091.	
	12.55	3270.	

Table 111. (con't)

$[\text{ClONO}_2]_0$ (10^{14} molecule cm^{-3})	N_2 density (10^{18} molecule cm^{-3})	ϕ_{NO_3}	Temperature (K)
7.00	0.353	141.5	298
	0.489	205.4	
	0.651	565.4	
	0.810	717.9	
	1.624	1515.	
	2.440	1839.	
	3.244	2137.	
	4.864	2540.	
	6.481	2895.	
10.0	0.519	564.8	298
	0.651	785.4	
	0.807	977.5	
	1.637	1894.	
	2.437	2254.	
	3.241	3240.	
	4.861	3167.	
	6.491	3239.	

Table IV. ClO and NO₃ product branching ratios.

Pressure (Torr)	[ClO] (10 ¹² molecule cm ⁻³)	Φ_{ClO}	[NO ₃] (10 ¹² molecule cm ⁻³)	Φ_{NO_3}
Pyrex cell photolysis				
[ClONO ₂] = 1.2 x 10 ¹⁴				
3.9	0.684	0.448	1.685	0.552
5.0	0.655	0.407	1.906	0.593
10.0	0.681	0.399	2.052	0.601
25.2	0.576	0.376	1.911	0.624
50.4	0.342	0.402	1.018	0.598
75.0	0.207	0.417	0.578	0.583
[ClONO ₂] = 2.5 x 10 ¹⁴				
10.0	1.643	0.477	3.596	0.523
25.2	1.319	0.419	3.653	0.581
50.2	0.664	0.447	1.643	0.553
75.1	0.357	0.483	0.765	0.517
[ClONCO ₂] = 3.2 x 10 ¹⁴				
10.0	2.335	0.472	5.327	0.528
25.4	2.142	0.459	5.265	0.541
50.0	0.889	0.472	1.818	0.528
75.1	0.372	0.487	0.649	0.513
Average	$\Phi_{\text{ClO}} = 0.44 \pm 0.07$		$\Phi_{\text{NO}_3} = 0.56 \pm 0.07$	
Quartz cell photolysis				
[ClONO ₂] = 1.3 x 10 ¹⁴				
5.5	4.789	0.628	5.683	0.372
10.3	4.697	0.598	6.316	0.402
25.2	3.728	0.585	5.289	0.415
50.3	3.153	0.638	3.573	0.622
75.3	2.745	0.663	2.787	
[ClONO ₂] = 2.5 x 10 ¹⁴				0.421
5.4	7.477	0.579	10.86	0.409
10.1	8.131	0.591	11.24	0.409
25.3	6.618	0.591	9.157	0.358
50.0	5.637	0.642	6.285	0.342
75.0	5.202	0.658	5.415	
[ClONO ₂] = 3.2 x 10 ¹⁴				
10.0	11.91	0.594	16.28	0.406
25.3	8.345	0.590	11.59	0.410
50.1	6.009	0.578	8.762	0.422
75.3	5.225	0.604	6.845	0.396
Average	$\Phi_{\text{ClO}} = 0.61 \pm 0.06$		$\Phi_{\text{NO}_3} = 0.39 \pm 0.06 \pm 0.06$	

Table V. Secondary reactions involving ClONO₂ photolysis products.

Reaction	Reaction Number	Rate coefficient (cm ³ molecule ⁻¹ s ⁻¹)	Ref.
ClONO ₂ $\xrightarrow{h\nu}$ ClO + NO ₂	1a	$\Phi_{\text{Pyrex}} = 0.44, \Phi_{\text{quartz}} = 0.61$	a
$\xrightarrow{h\nu}$ Cl + NO ₃	1b	$\Phi_{\text{Pyrex}} = 0.56, \Phi_{\text{quartz}} = 0.39$	a
$\xrightarrow{h\nu}$ ClONO + O	1c	$\Phi \leq 0.04$	8
Cl + ClONO ₂ \longrightarrow Cl ₂ + NO ₃	2	$k_{298} = 1.0 \times 10^{-11}$	14
O + ClONO ₂ \longrightarrow ClO + NO ₃	3	$k_{298} = 2.0 \times 10^{-13}$	14
ClO + NO ₂ \xrightarrow{M} ClONO ₂	4	$k_{298} = 1.8 \times 10^{-31,c}$	14
ClO + NO ₃ \longrightarrow OClO + NO ₂	5	$k_{298} = 4.7 \times 10^{-13}$	14
Cl + NO ₃ \rightarrow ClO + NO ₂	6	$k_{298} = 2.4 \times 10^{-11}$	14
Cl + NO ₂ \xrightarrow{M} ClONO	7	$k_{298} = 1.3 \times 10^{-30,c}$	14
NO ₂ + NO ₃ \xrightarrow{M} N ₂ O ₅	8	$k_{298} = 2.2 \times 10^{-30,c}$	14
Cl + ClONO \longrightarrow Cl ₂ + NO ₂	9	$k_{298} \approx 2.0 \times 10^{-11}$	9
ClO + ClO \xrightarrow{M} Cl ₂ O ₂	10a	$k_{298,N_2} = 2.0 \times 10^{-32,c}$	5
ClO + ClO \longrightarrow Cl ₂ + O ₂	10b	$k_{298} = 4.9 \times 10^{-15}$	5
\longrightarrow ClOO + Cl	10c	$k_{298} = 8.0 \times 10^{-15}$	5
\longrightarrow OClO + Cl	10d	$k_{298} = 3.5 \times 10^{-15}$	5
Cl ₂ O ₂ \xrightarrow{M} 2ClO	11	$k_{298} = 3.0 \times 10^{-18}$	5
Cl + Cl ₂ O ₂ \longrightarrow Cl ₂ + ClOO	12	$k_{298} = 1.0 \times 10^{-10}$	4
Cl + ClOO \longrightarrow Cl ₂ + O ₂	13a	$k_{298} = 2.3 \times 10^{-10}$	4
\longrightarrow 2ClO	13b	$k_{298} = 1.2 \times 10^{-11}$	4
Cl + OClO \longrightarrow 2ClO	14	$k_{298} = 5.8 \times 10^{-11}$	4
ClOO \xrightarrow{M} Cl + O ₂	15	$k_{298} = 1.1 \times 10^{-12}$	4
Cl + O ₂ \xrightarrow{M} ClOO	16	$k_{298} = 2.7 \times 10^{-33,c}$	4

This work.

b) Estimated from rate constants for Cl + ClONO₂ and Cl + ClNO

c) units of cm⁶ molecule⁻² s⁻¹

Figure Captions

Figure 1. Spectral distributions of the xenon flashlamp with different cell/filter solution combinations: (a) quartz, cell; (b) Pyrex ccl]; (c) Pyrex cell with $\text{CrK}(\text{SO}_4)_2 \cdot 12\text{H}_2\text{O}$ (100 g l.⁻¹) filter solution; (d) Pyrex ccl] with $\text{Ce}(\text{NH}_4)_2(\text{NO}_3)_6$ (5 g l.⁻¹) filter solution.

Figure 2. The uv-visible absorption spectrum of ClONO_2 from ref. 14. Bars at bottom of plot indicate spectral regions excited by different cell/filter combinations.

Figure 3. NO_3 temporal signals recorded with the OMA spectrometer following photolysis in the Pyrex cell at total pressures of: (a) 10.3 '1'err; (b) 25.3 '1'or-r; (c) 50.1 "1'err; and (d) 100.1 Torr. Bath gas was N_2 , $[\text{ClONO}_2]_0 = 1 \times 10^{14}$ molecule cm^{-3} , and '1' = 298 K.

Figure 4. NO_3 temporal signals recorded with the PMT spectrometer following photolysis in the Pyrex ccl] at total pressures of: (a) 10.2 '1'err; (b) 15.2 '1'err; (c) 25.1 '1'err; and (d) 50.3 "1'm-r. Bath gas was N_2 , $[\text{ClONO}_2]_0 = 2 \times 10^{14}$ molecule cm^{-3} , and 'J' = 298 K.

Figure 5. ClO temporal signals recorded with the OMA spectrometer following photolysis in the Pyrex ccl] at total pressures of: (a) 5.1 '1'err; (b) 10.1 '1'err; (c) 15.1 '1'err; (d) 24.9 '1'err; and (e) 50.4 Torr. Bath gas was N_2 , $[\text{ClONO}_2]_0 = 1 \times 10^{14}$ molecule cm^{-3} , and T = 298 K.

Figure 6. ClO temporal signals recorded with the PMT spectrometer following photolysis in the Pyrex cell at total pressures of: (a) 12.8 Torr ($[\text{N}_2] = 0.0$ molecule cm^{-3}); (b) 15.1 Torr ($[\text{N}_2] = 0.789 \times 10^{17}$ molecule cm^{-3}); and (c) 20.1 Torr ($[\text{N}_2] = 2.41 \times 10^{17}$ molecule cm^{-3}). $[\text{ClONO}_2]_0 = 4 \times 10^{14}$ molecule cm^{-3} , and T = 298 K.

Figure 7. NO_3 temporal signals recorded with the OMA spectrometer following photolysis in the quartz ccl] at total pressures of: (a) 5 '1'err; (b) 100 Torr; and (c) 400 Torr. Dashed lines are a fit of the data to a Stern-Volmer type mechanism that also included product secondary chemistry. Bath gas was N_2 , $[\text{ClONO}_2]_0 = 1 \times 10^{14}$ molecule cm^{-3} , and T = 298 K.

Figure 8. NO_3 temporal signals recorded with the PMT spectrometer following photolysis in the quartz cell at total pressures of: (a) 10.2 Torr; (b) 25.1 Torr; (c) 50.3 '1'err; (d) 100.6 '1'err; and (e) 200.0 Torr. Bath gas was helium, $[\text{ClONO}_2]_0 = 6.5 \times 10^{14}$ molecule cm^{-3} , and T = 298 K.

Figure 9. ClONO₂ temporal signals measured with the PMT spectrometer at 225 nm following photolysis in the Pyrex cell. Total pressures are: (a) 3.2 Torr ([N₂] = 0.0 molecule cm⁻³); (b) 5.1 Torr ([N₂] = 0.616 × 10¹⁷ molecule cm⁻³); and (c) 15.1 Torr ([N₂] = 3.80 × 10¹⁷ molecule cm⁻³). [ClONO₂]₀ = 1 × 10¹⁴ molecule cm⁻³, and T = 298 K.

Figure 10. Relative NO₃ yield as a function of N₂ density for photolysis in the Pyrex cell. Solid symbols are from the PMT data; open symbols are from the OMA data. [ClONO₂]₀ = 1 × 10¹⁴ molecule cm⁻³, and T = 298 K.

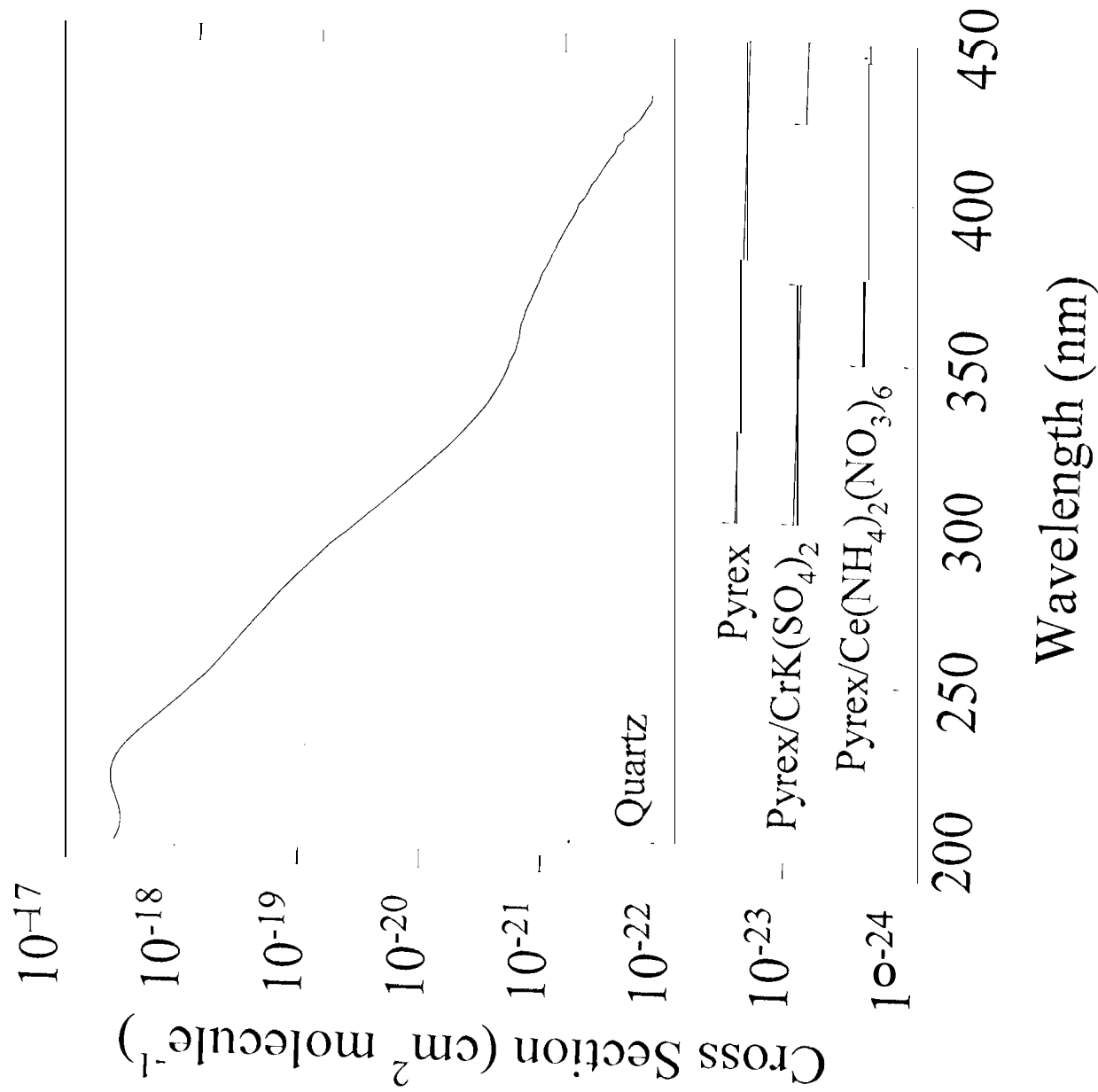
Figure 11. Comparison of NO₃ and ClO product yields as a function of N₂ density for photolysis in the Pyrex cell. Solid symbols are for NO₃; open symbols are for ClO. Initial chlorine nitrate concentrations are: (●) 2.5 × 10¹³ molecule cm⁻³; (■) 5.0 × 10¹³ molecule cm⁻³; (▲) 7.5 × 10¹³ molecule cm⁻³; and (◆) 1.0 × 10¹⁴ molecule cm⁻³.

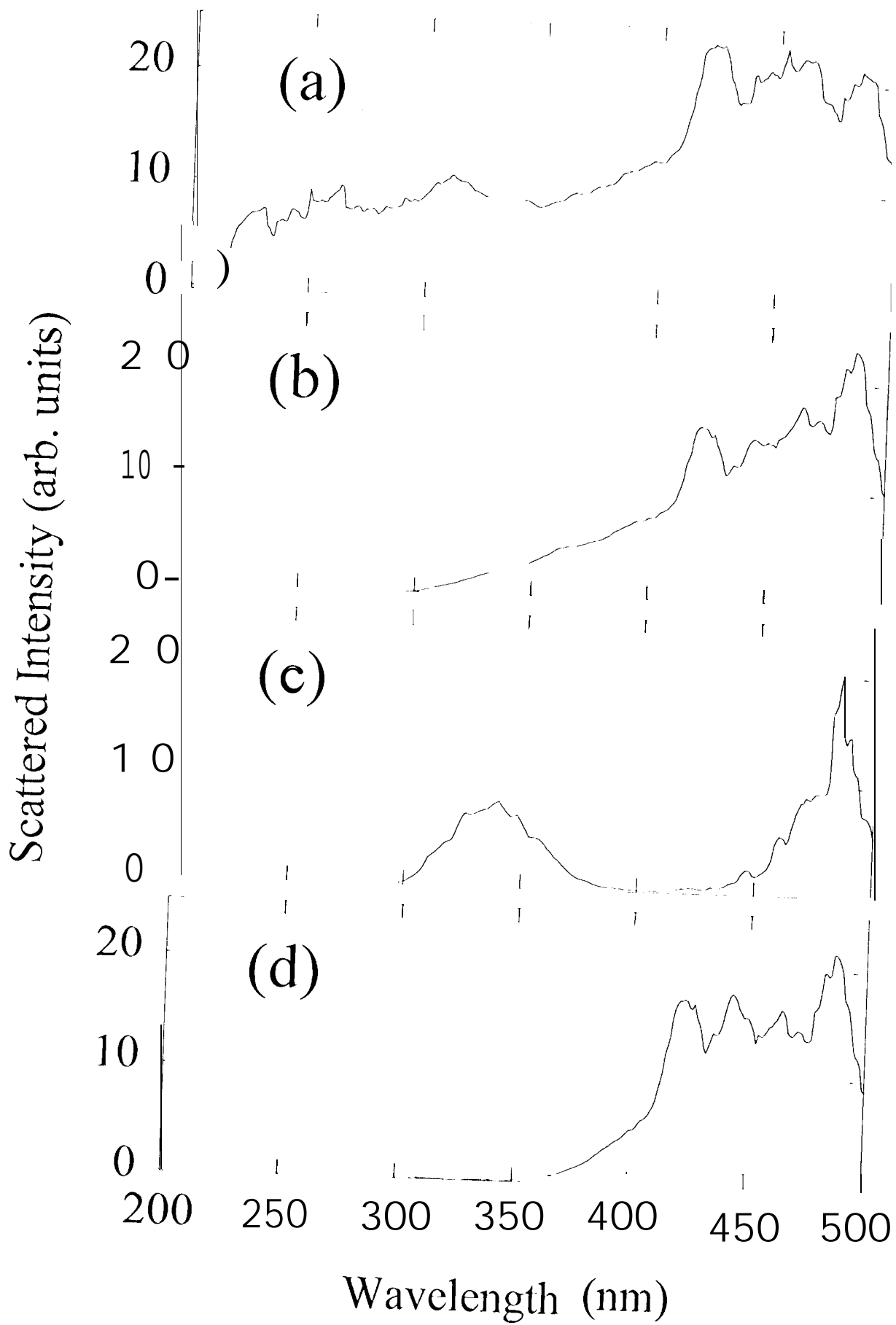
Figure 12. NO₃ product yield as a function of air density for the four cell/filter solution combinations. (○) unfiltered quartz cell; (V) unfiltered Pyrex cell; (O) Pyrex cell with CrK(SO₄)₂·12H₂O filter solution; (∧) Pyrex cell with Ce(NH₄)₂(NO₃)₆ filter solution. Solid lines are empirical fits to each data set and are provided as a visual guide.

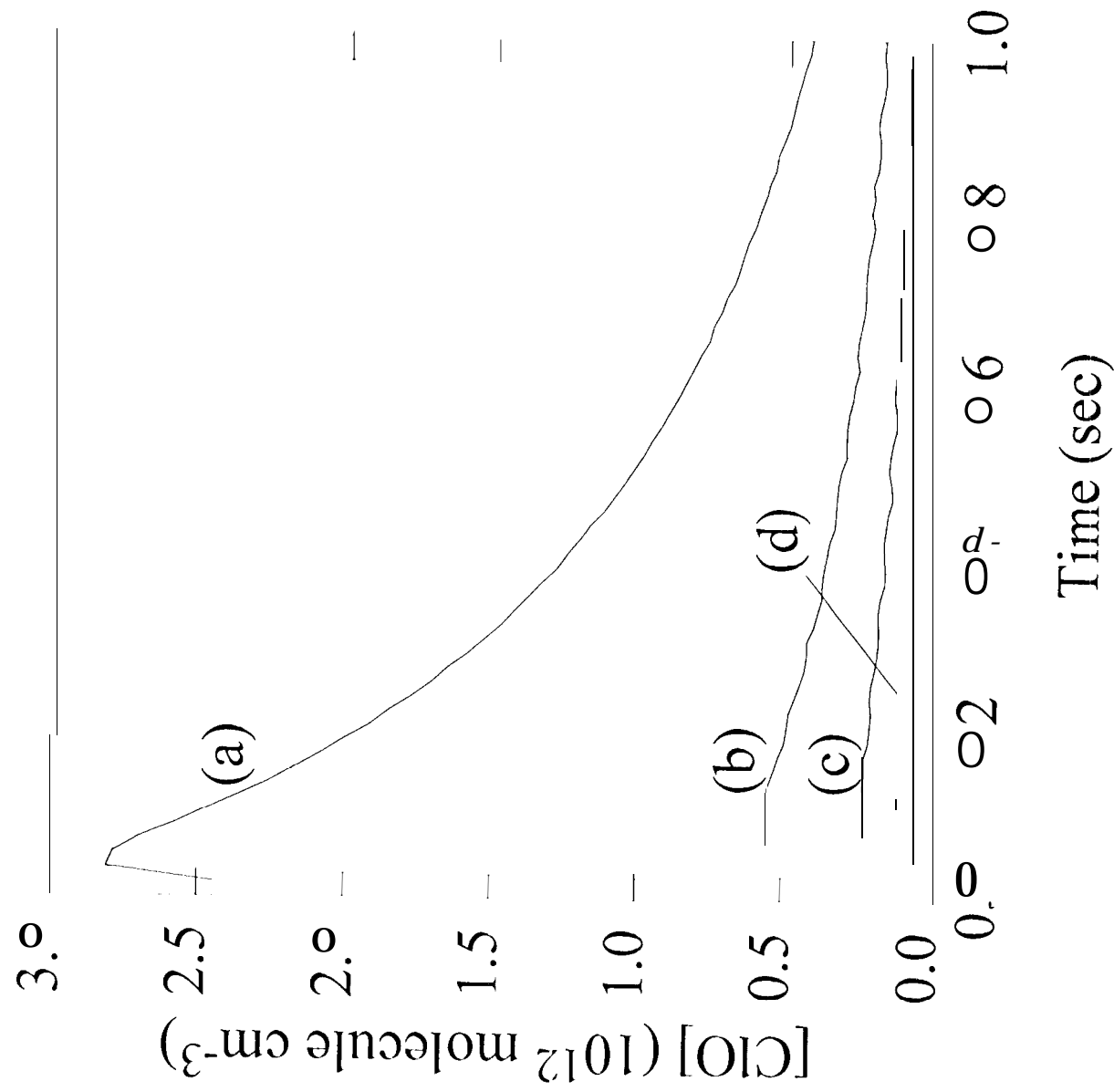
Figure 13. inverse NO₃ product yield as a function of N₂ density and initial chlorine nitrate concentration. Initial concentrations are: (●) 2.5 × 10¹³ molecule cm⁻³; (○) 5.0 × 10¹³ molecule cm⁻³; (■) 7.5 × 10¹³ molecule cm⁻³; (□) 7.5 × 10¹³ molecule cm⁻³ (220 K); (▲) 1.0 × 10¹⁴ molecule cm⁻³; (∧) 2.0 × 10¹⁴ molecule cm⁻³; (◆) 3.0 × 10¹⁴ molecule cm⁻³; (◇) 4.0 × 10¹⁴ molecule cm⁻³; (♦) 7.0 × 10¹⁴ molecule cm⁻³; and (∇) 1.0 × 10¹⁵ molecule cm⁻³. Temperature was 298 K unless otherwise indicated.

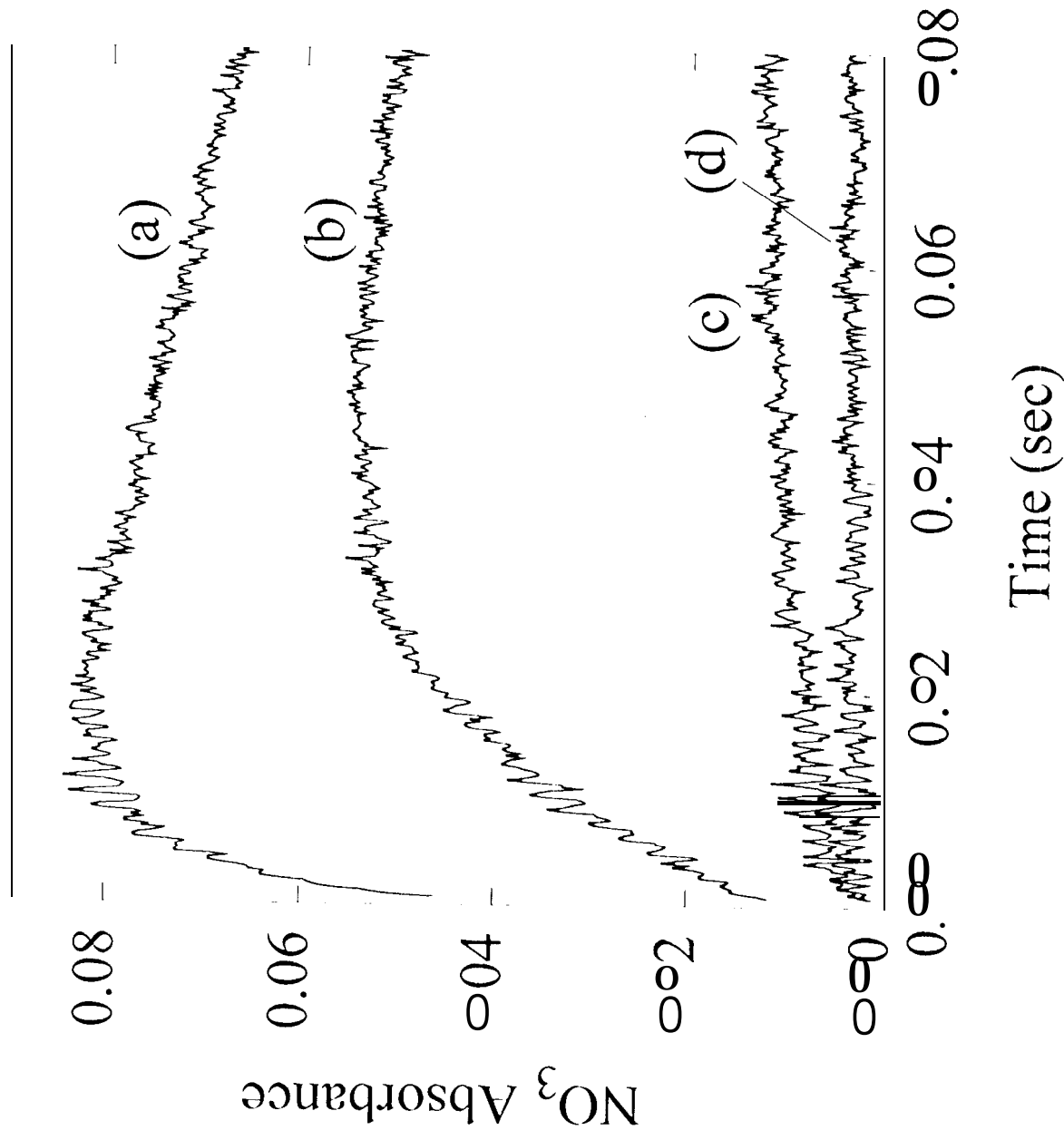
Figure 14. Simulations of the NO₃ data for photolysis in the unfiltered Pyrex cell using a mechanism that includes quenching to and dissociation from a metastable intermediate as well as the product secondary chemistry outlined in Table V. Total pressures are: (a) 5 Torr; (b) 10 Torr; (c) 25 Torr; and (d) 100 Torr.

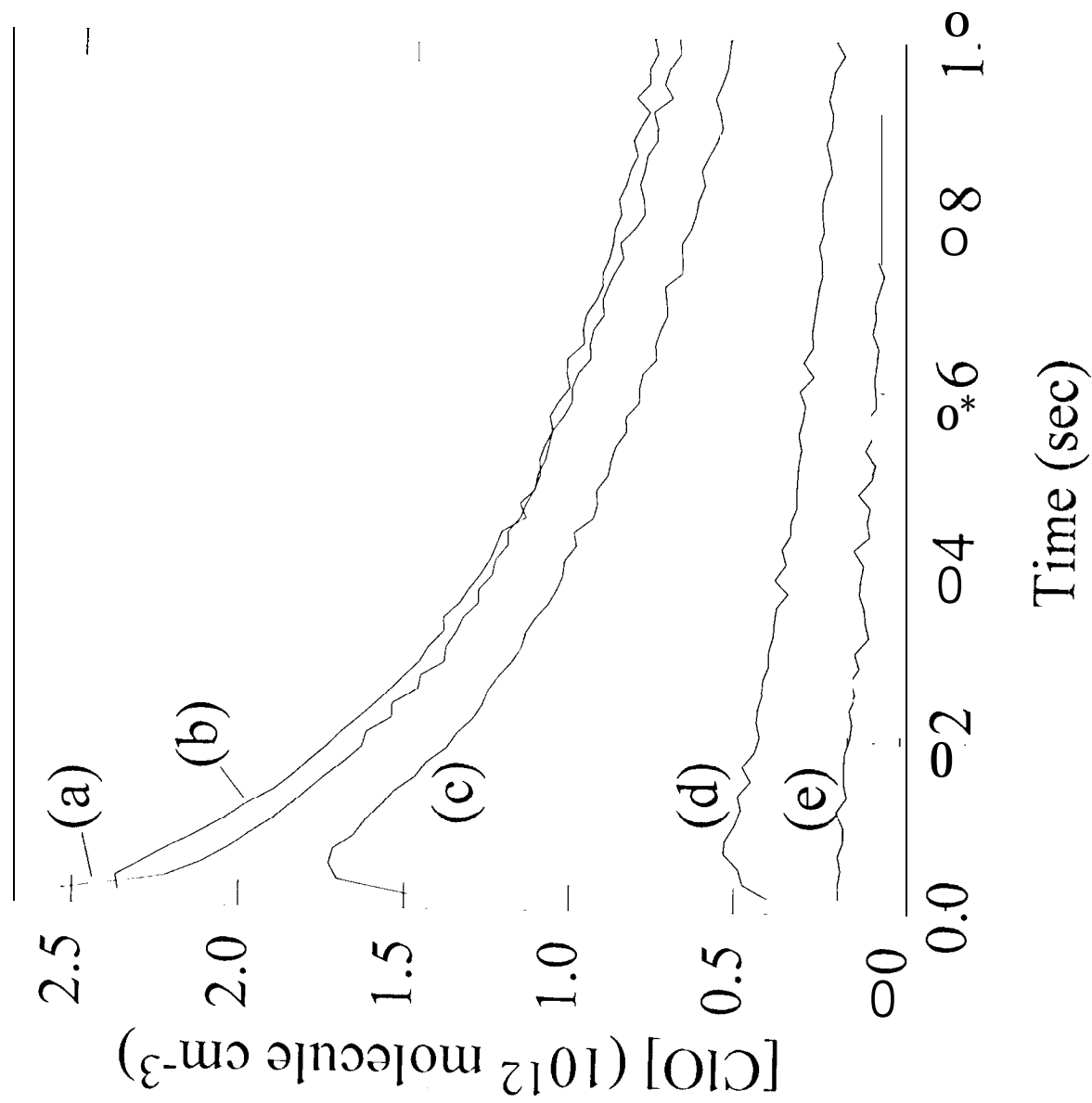
Figure 15. Vertical excitation energies of the excited electronic states of chlorine nitrate adapted from reference 10.

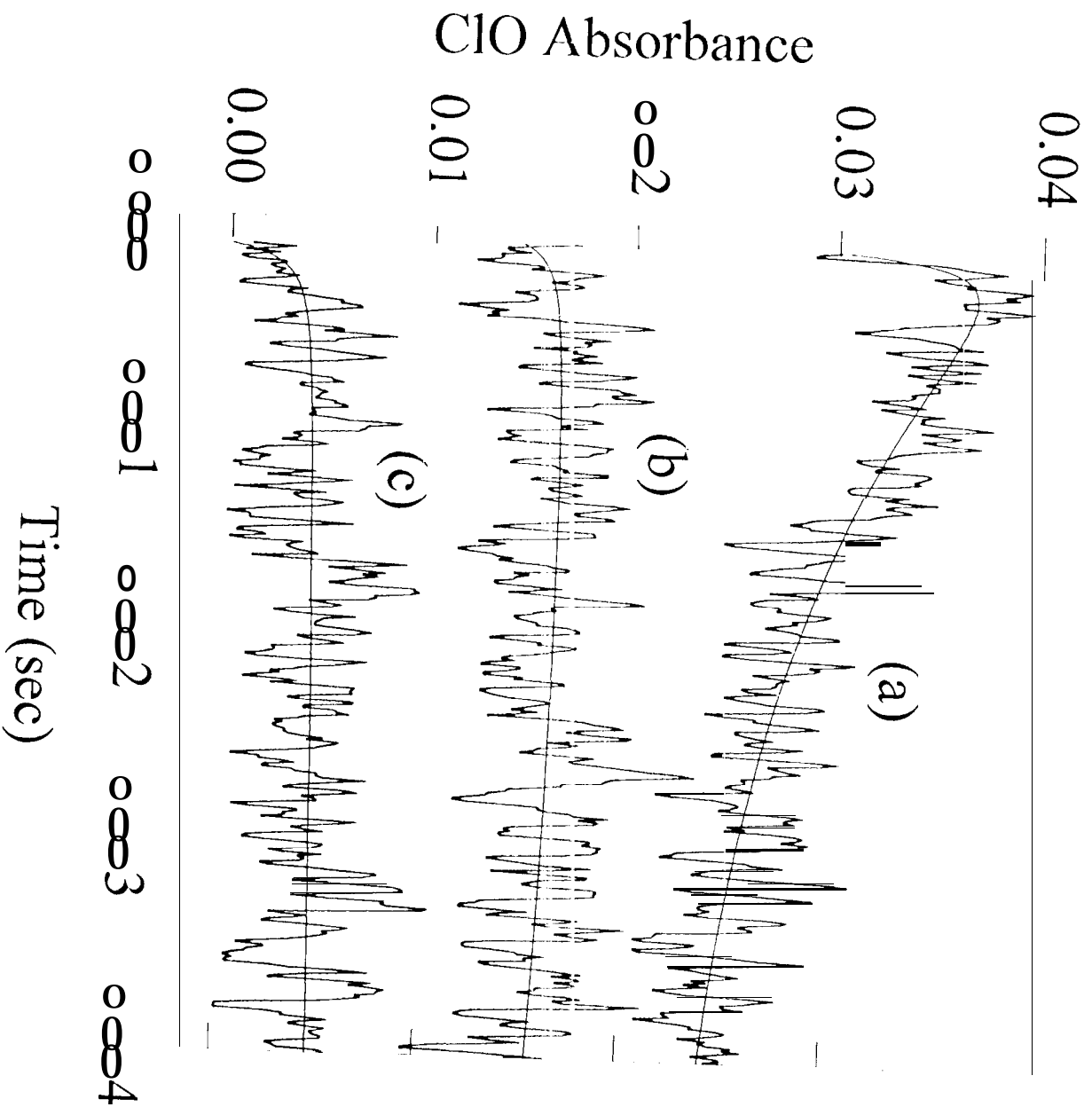


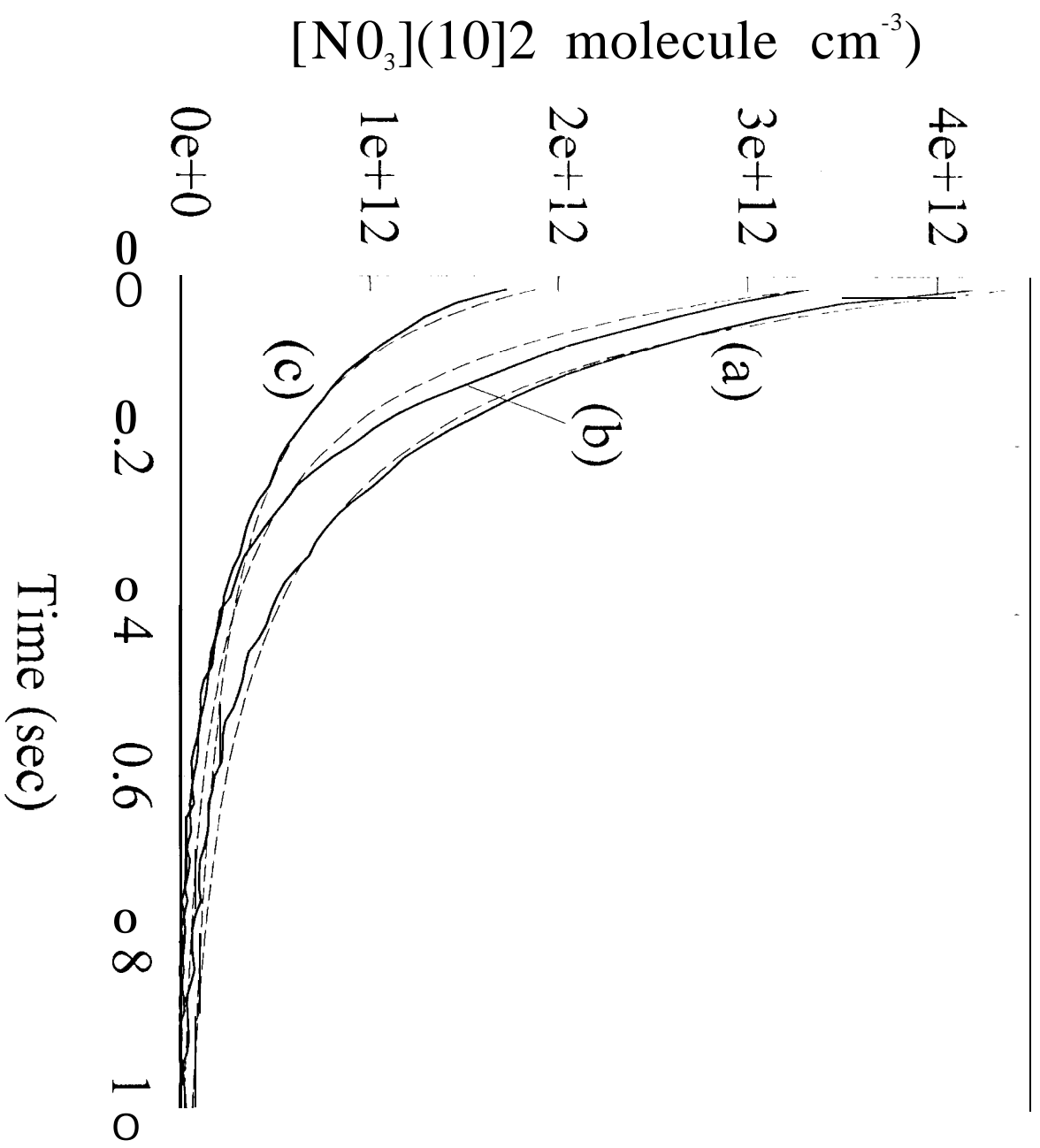


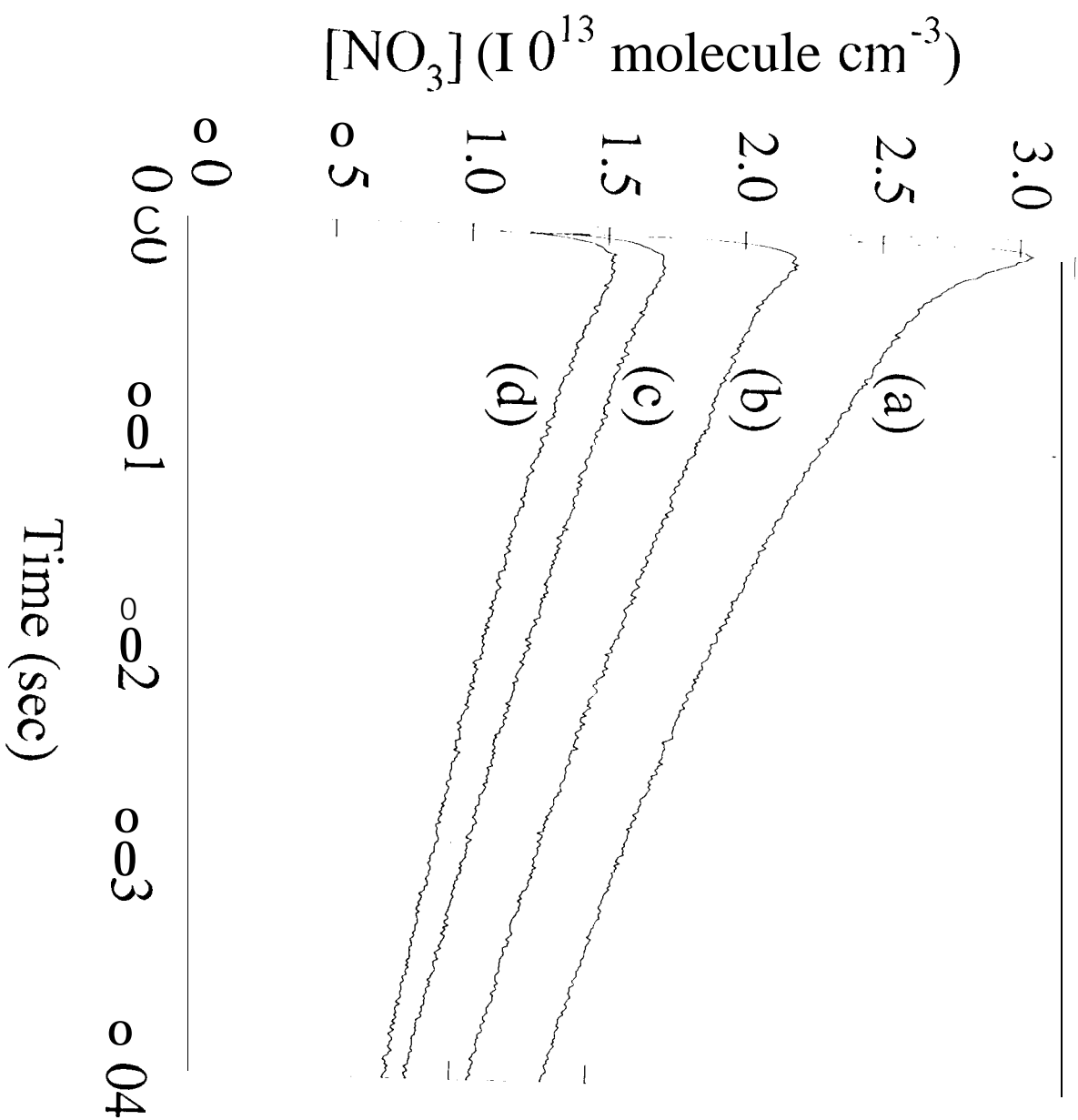












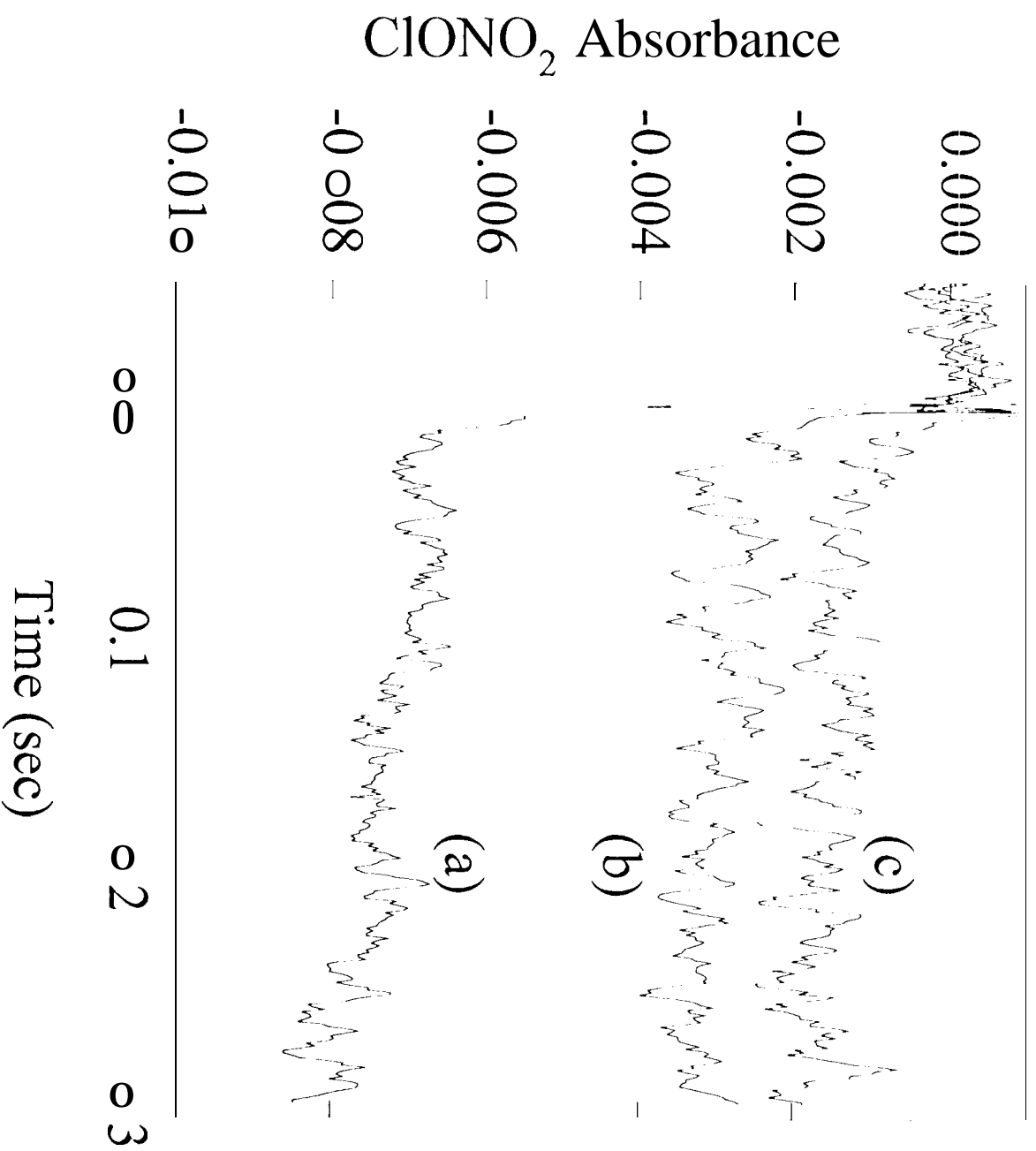


Fig. 4

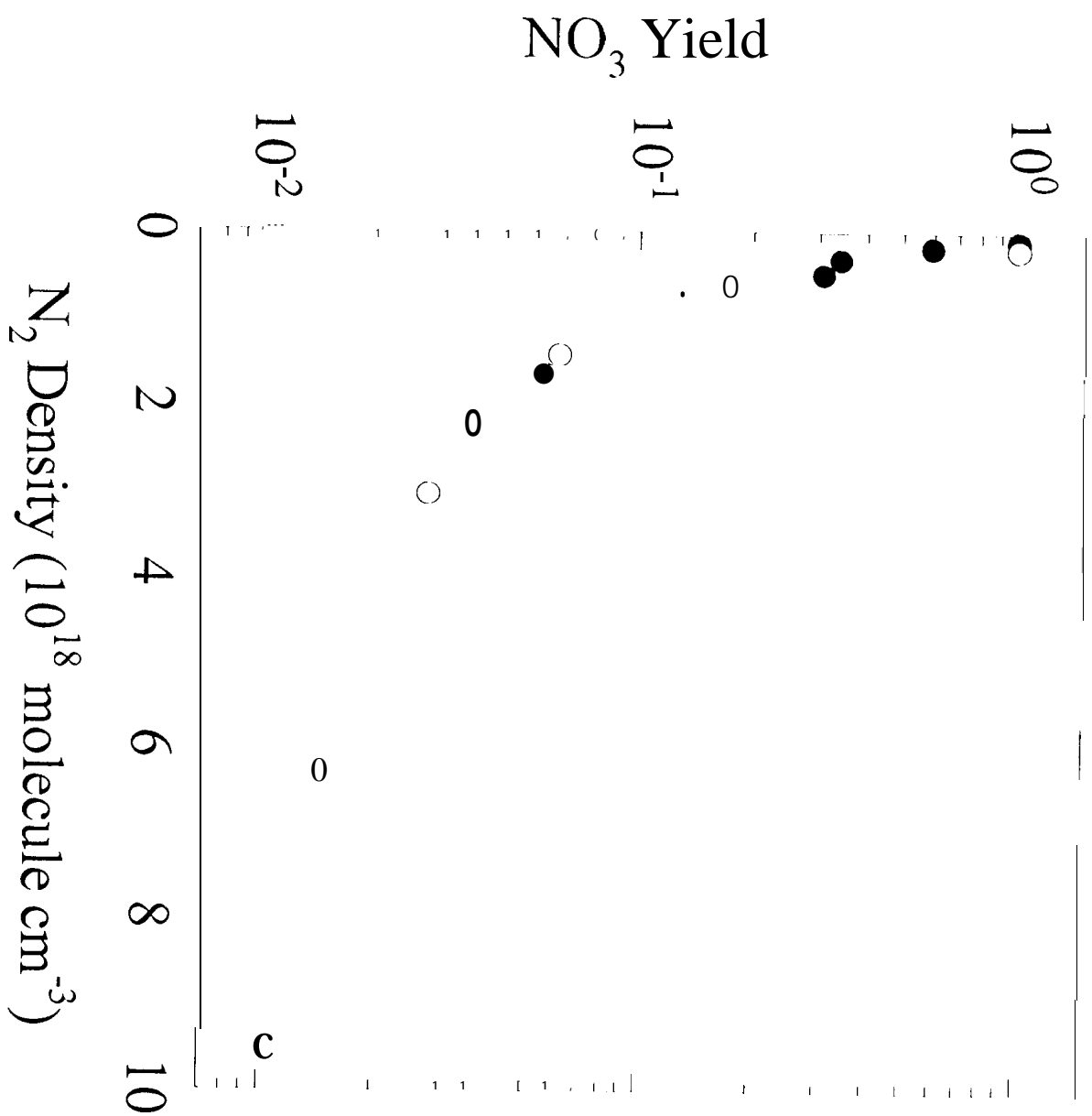


Fig. 10

